
A FREQUENCY-DOMAIN DIFFERENTIAL CORRECTOR FOR QUASI-PERIODIC TRAJECTORY DESIGN AND ANALYSIS

Beom Park

PhD Candidate
School of Aeronautics and Astronautics
Purdue University
West Lafayette, IN, USA, 47906
park1103@purdue.edu

Kathleen C. Howell

Hsu Lo Distinguished Professor
School of Aeronautics and Astronautics
Purdue University
West Lafayette, IN, USA, 47906
howell@purdue.edu

Shaun Stewart

Flight Dynamics Lead
Intuitive Machines
Houston, TX, USA, 77059
sstewart@intuitivemachines.com

ABSTRACT

This paper introduces the Frequency-Domain Differential Corrector (FDDC), a model-agnostic approach for constructing quasi-periodic orbits (QPOs) across a range of dynamical regimes. In contrast to existing methods that explicitly enforce an invariance condition in all frequency dimensions, the FDDC targets dominant spectral components identified through frequency-domain analysis. Leveraging frequency refinement strategies such as Laskar-Numerical Analysis of Fundamental Frequency (L-NAFF) and Gómez-Mondelo-Simó-Collocation (GMS-C), the method enables efficient and scalable generation of high-dimensional QPOs. The FDDC is demonstrated in both single- and multiple-shooting formulations. While the study focuses on the Earth–Moon system, the framework is broadly applicable to other celestial environments. Sample applications include Distant Retrograde Orbits (DROs), Elliptical Lunar Frozen Orbits (ELFOs), and Near Rectilinear Halo Orbits (NRHOs), illustrating constellation design and the recovery of analog solutions in higher-fidelity models. With its model-independent formulation and spectral targeting capabilities, FDDC offers a versatile tool for robust trajectory design and mission planning in complex dynamical systems.

1 Introduction

Periodic and quasi-periodic trajectories serve as a fundamental framework in astrodynamics. Closely linked to the integrability of a system, these structures illuminate the architecture of the phase space and provide a basis for understanding long-term orbital behaviors. For instance, the classical two-body problem, comprising a point-mass central body and a spacecraft, is a superintegrable system in the Liouville-Arnold sense [1], with five independent integrals of motion within a three degree-of-freedom Hamiltonian system. Its solutions emerge as the conic sections including the ellipses as the fundamental periodic structures, undoubtedly serving as basis for astrodynamics. When perturbations are introduced, often rendering the system non-integrable, new behaviors such as chaos may emerge. Nonetheless, many periodic and quasi-periodic structures persist. The Circular Restricted Three-Body Problem (CR3BP), describing a spacecraft under the gravitational

influence of two primary bodies, serves as a canonical example for such a non-integrable system. Typically represented within a rotating frame, it retains only a single integral of motion, the Jacobi constant [2]. Despite its non-integrability, the CR3BP admits a wealth of (quasi-)periodic orbits, including those near each primary and various resonant orbits, as well as families of orbits near the Lagrange points [3, 4].

The (quasi-)periodic orbits play a critical role in both theoretical and applied contexts in astrodynamics. In particular, periodic orbits in the CR3BP exist in continuous one-parameter families [3]. Linearized dynamics around the periodic orbit allow bifurcation analysis [5] and aid in characterizing the invariant manifolds that govern the nearby phase space [6, 7]. In the planar CR3BP, for example, the hyperbolic manifolds associated with Lyapunov orbits around the L_1 and L_2 Lagrange points are responsible for organizing global transport and giving rise to chaotic motion through homoclinic tangles [8, 9, 10]. Beyond their utility in illustrating the global phase space, specific (quasi-)periodic orbits are often well-suited for mission design, offering useful properties such as repeated ground tracks, reduced eclipse exposure, constant line-of-sight, or proximity to regions of interest, such as the lunar south pole. Notable mission-relevant examples include the Near Rectilinear Halo Orbit (NRHO) and the Distant Retrograde Orbit (DRO), underpinning key components of NASA’s Gateway architecture [11].

Despite the utility of (quasi-)periodic orbits in the CR3BP, identifying suitable counterparts in higher-fidelity models remains a significant challenge. As noted by Jorba and Villanueva [12], an n_i -dimensional quasi-periodic orbit (QPO) in the CR3BP generally evolves into an $(n = n_i + n_e)$ -dimensional QPO in a higher-fidelity model, with the additional n_e frequencies inherited (external) from perturbations. For the CR3BP, $n_i \leq 3$, as a 3 degree-of-freedom Hamiltonian system. However, the number of inherited frequencies n_e may be significant. For example, within the Earth-Moon system, at least five distinct frequencies ($n_e \geq 5$) are typically required to capture key perturbations, including Earth-Moon distance variations and solar effects [13].

The current investigation focuses on developing numerical strategies to construct higher-dimensional quasi-periodic trajectories that occur frequently within more realistic dynamical environments. The increase in dimensionality poses challenges for existing numerical schemes. Baresi, Olikara, and Scheeres [14] review several fully-numerical approaches, with an algorithm proposed by Gómez and Mondelo [15] and refined by Olikara and Scheeres [16] (GMOS) serving as the de facto standard due to its advantages in computational speed and accuracy. However, GMOS and similar strategies face the “curse of dimensionality,” where the cost of supplying high-dimensional QPOs scales poorly due to the need to invert large, dense matrices [17]. To date, this method has been verified primarily for $n = n_i + n_e \leq 3$ [18, 19, 20, 21], and while extensions are possible, computational requirements quickly become intractable as n increases. An alternative approach proposed by Haro and Mondelo [22], termed the Flow Map Parametrization (FMP), circumvents some of these limitations by replacing the dense matrix inversion with a quasi-Newton iteration. The method is semi-analytical and leverages quasi-Floquet theory [23] for an alternative basis. Although FMP significantly reduces computational cost and has been demonstrated and extended to the Elliptic Restricted Three-Body Problem (ER3BP) [24, 17] and the Hill Restricted Four-Body Problem (HR4BP) [25, 26], its implementation is more complex compared to the GMOS algorithm. The examples that appear in the literature discuss $n \leq 3$. Whether the method scales effectively to larger values of n remains an open question. Both GMOS and FMP aim to explicitly construct the n -dimensional QPO directly. Although the methods are formally generalizable, their reliance on model-specific derivations may pose a barrier to broader adoption and practical application.

Proposed in this paper is a complementary approach to deliver n -dimensional QPOs, termed the Frequency-Domain Differential Corrector (FDDC). The strategy acknowledges that the n_e inherited frequencies are dictated by external forcing and are not directly controllable. By leveraging frequency-domain information, specifically the correction of dominant spectral peaks, the strategy introduces a differentiable update process informed by previous work on frequency analysis [27, 28]. Thus, rather than explicitly enforcing the invariance condition in all n dimensions, the FDDC corrects for the intrinsic n_i frequency components. The FDDC method is intended as a more computationally tractable strategy for constructing high-dimensional QPOs in complex dynamical environments. Moreover, the approach is model-agnostic: the same formulation is adaptable across a variety of dynamical models without requiring significant modification. These features make the FDDC strategy well-suited for generating baseline solutions for long-duration missions such as Gateway, or for maintaining constellations of spacecraft with constraints on relative phasing and geometry.

The remainder of the document is organized as follows. Section 2 introduces representative dynamical models within the Earth-Moon system, although the proposed method is applicable to any other regimes as well. Foundational tools in frequency analysis are explored in Section 3 that motivate the corrections strategy. In Section 4, the single-shooting formulation of the FDDC strategy is presented, along with demonstrations involving Distant Retrograde Orbits (DROs) and Elliptical Lunar Frozen Orbits (ELFOs). The algorithm is extended in Section 5 to a multiple-shooting formulation, with an application to a 9 : 2 synodic resonant halo orbit. Concluding remarks are provided in Section 6.

2 Preliminaries: Frames, Dynamical Models, and Quasi-Periodic Orbits (QPOs)

The Frequency-Domain Differential Corrector (FDDC) is designed to be model-agnostic, and its implementation is demonstrated using three representative dynamical models in the Earth-Moon system: the Doubly-Averaged Dynamical Model (DADM), the Circular Restricted Three-Body Problem (CR3BP), and a Higher-Fidelity Ephemeris Model (HFEM). These models span a hierarchy of fidelity levels and illustrate the scalability of the proposed approach. The following subsections detail the coordinate systems, frame transformations, and governing equations for each model.

2.1 Frames and Transformations

To support analyses across these models, three reference frames are employed. Each frame plays a distinct role in state propagation, element extraction, and frame-to-frame transformation. These various frames facilitate analyses of various structures as follows:

(Frame 1) Barycentric Rotating Frame (BRF): this frame adopts an orthogonal basis $\hat{x} - \hat{y} - \hat{z}$ defined as follows: (1) \hat{x} is directed from the Earth to the Moon, (2) \hat{z} coincides with the angular momentum of the Moon in its orbit with respect to Earth, and (3) \hat{y} completes the dextral triad. The origin of the frame is located at the Earth-Moon barycenter. With the Earth-Moon distance normalized to be unity (regardless of the actual dimensional distance), this frame renders fixed locations for the Earth and Moon along the \hat{x} axis at $-\mu$ and $(1 - \mu)$. The mass ratio μ measures the ratio of the mass of the Moon with respect to the Earth-Moon system mass. The nondimensional (nd) spacecraft position vector is expressed as $\vec{\rho} = x\hat{x} + y\hat{y} + z\hat{z}$.

(Frame 2) Moon-Centered Earth Orbit Frame (EOF): the orthonormal basis $\hat{X}_E - \hat{Y}_E - \hat{Z}_E$ is constructed such that \hat{Z}_E coincides with \hat{z} , and $\hat{X}_E - \hat{Y}_E$ are produced by rotating $\hat{x} - \hat{y}$ at a constant negative rate with respect to \hat{Z} . The origin of the frame is located at the center of the Moon. The nd spacecraft position vector within the EOF is then constructed as,

$$\vec{R}_E = \mathbf{C}_E(\vec{\rho} - \vec{\rho}_M) = X_E\hat{X}_E + Y_E\hat{Y}_E + Z_E\hat{Z}_E, \quad \mathbf{C}_E = \begin{bmatrix} \cos(t) & -\sin(t) & 0 \\ \sin(t) & \cos(t) & 0 \\ 0 & 0 & 1 \end{bmatrix}, \quad (1)$$

where $\rho_M = (1 - \mu)\hat{x}$, the nd lunar position vector within the BRF. The nd time t is constructed leveraging the characteristic quantities l_* and t_* defined as the average Earth-Moon distance and $t_* = \sqrt{l_*^3/(\tilde{\mu}_E + \tilde{\mu}_M)}$ where $\tilde{\mu}_{E,M}$ are the dimensional gravitational parameters for the Earth and Moon, respectively. Then, t normalizes the dimensional time via t_* . It is assumed that, at $t = 0$, the Earth is on the positive \hat{X}_E -axis without losing generality. This frame is defined consistent with previous investigations [29, 30, 31]. For the nd position and velocity, i.e., $\vec{R}_E, \vec{R}'_E = d\vec{R}_E/dt$, the osculating orbital elements α with respect to the Moon are retrieved leveraging standard transformation schemes, e.g., in Vallado [32], i.e., $\alpha = \alpha(\vec{R}_E, \vec{R}'_E)$. The classical Keplerian elements are adopted in the current investigation as follows: a (semi-major axis), e (eccentricity), i (inclination), ω (argument of perilune), Ω (right ascension of the ascending node), and M (mean anomaly). To facilitate analysis for regions in the vicinity of the Moon, it is common practice to *average* the perturbations from the Earth along the lunar orbit with respect to both M and Ω . This process results in the *doubly-averaged* mean orbital elements, $\bar{\bar{\alpha}}$, where the double bar indicates the quantity is averaged twice.

(Frame 3) Moon-Centered J2000 Inertial Frame (JIF): the unit vectors $\hat{X} - \hat{Y} - \hat{Z}$ are defined consistent with the J2000 inertial frame. The nd spacecraft position vector in the frame is rendered as [33],

$$\vec{R} = \frac{l}{l_*} \mathbf{C}(\vec{\rho} - \vec{\rho}_M) = X\hat{X} + Y\hat{Y} + Z\hat{Z}, \quad \mathbf{C} = [\hat{x} \quad \hat{y} \quad \hat{z}], \quad (2)$$

where l, l_* are the instantaneous and mean Earth-Moon distances, respectively. The unit vectors $\hat{x} - \hat{y} - \hat{z}$ are constructed instantaneously based on the numerical ephemerides DE440 [34]. Building upon these frames, the transformations between the various state representations are summarized in Fig. 1. The transformation between doubly-averaged mean elements, $\bar{\bar{\alpha}}$, and osculating elements, α , is a non-trivial process in general, where a suitable transformation depends on the instantaneous configurations in the system. In the current investigation, however, $\bar{\bar{\alpha}} = \alpha$, i.e., both elements are treated equivalently. Such an approximation is justified from the fact that any semi-analytical transformation between $\bar{\bar{\alpha}}$ and α still requires further refinement. This work focuses on the refinement algorithm itself, alleviating the dependency on an accurate transformation between $\bar{\bar{\alpha}}$ and α . The rest of the transformations in Fig. 1 are provided more trivially via Eqs. (1)-(2). Note that the velocities, i.e., $\vec{R}'_E, \vec{\rho}', \vec{R}'$, are interdependent via derivatives for these equations.



Fig. 1: Transformations across various state representations and frames

2.2 Doubly-Averaged Dynamical Model (DADM)

Within the Moon-dominated dynamical regime, several assumptions are introduced to supply the DADM that is employed in the current investigation. Firstly, the point-mass Earth is the only perturbing body. While it is possible to extend the DADM to include the perturbations from the nonspherical gravity from the Moon [35], such extensions are not considered here as the focus remains on the regions where the most dominant perturbations originate from the Earth [30]. Then, the Earth's perturbing potential is truncated leveraging the Legendre expansion as detailed by Longuski et al. [36]. Subsequently, the perturbation from the Earth is averaged over (1) Ω and (2) M to supply the doubly-averaged, truncated Earth perturbing potential,

$$\bar{\bar{P}} = \frac{1}{32} n_E \bar{\bar{a}}^2 \left[(1 + 3 \cos 2\bar{\bar{i}})(2 + 3\bar{\bar{e}}^2) + 30\bar{\bar{e}}^2 \sin^2 \bar{\bar{i}} \cos 2\bar{\bar{\omega}} \right]. \quad (3)$$

where n_E is the dimensional mean angular rate for the Earth around the Moon. Recall that the doubly-averaged mean elements, i.e., $\bar{\bar{\alpha}}$, are supplied within the EOF. From Lagrange's planetary equations, the mean orbital elements evolve at the following rates [29, 35, 31],

$$\frac{d\bar{\bar{a}}}{dt} = 0 \quad (4)$$

$$\frac{d\bar{\bar{e}}}{dt} = \frac{15}{8} \frac{(1 - \mu) n_E^2 t_*}{\bar{\bar{n}}} \bar{\bar{e}} (1 - \bar{\bar{e}}^2)^{1/2} \sin^2 \bar{\bar{i}} \sin 2\bar{\bar{\omega}} \quad (5)$$

$$\frac{d\bar{\bar{i}}}{dt} = -\frac{15}{16} \frac{(1 - \mu) n_E^2 t_*}{\bar{\bar{n}}} \frac{\bar{\bar{e}}^2}{(1 - \bar{\bar{e}}^2)^{1/2}} \sin 2\bar{\bar{i}} \sin 2\bar{\bar{\omega}} \quad (6)$$

$$\frac{d\bar{\bar{\omega}}}{dt} = \frac{3}{16} \frac{(1 - \mu) n_E^2 t_*}{\bar{\bar{n}}} \frac{1}{(1 - \bar{\bar{e}}^2)^{1/2}} \left[(3 + 2\bar{\bar{e}}^2 + 5 \cos 2\bar{\bar{i}}) + 5(1 - 2\bar{\bar{e}}^2 - \cos 2\bar{\bar{i}}) \cos 2\bar{\bar{\omega}} \right] \quad (7)$$

$$\frac{d\bar{\bar{\Omega}}}{dt} = \frac{3}{8} \frac{(1 - \mu) n_E^2 t_*}{\bar{\bar{n}}} \frac{1}{(1 - \bar{\bar{e}}^2)^{1/2}} (5\bar{\bar{e}}^2 \cos 2\bar{\bar{\omega}} - 3\bar{\bar{e}}^2 - 2) \cos \bar{\bar{i}} \quad (8)$$

$$\frac{d\bar{\bar{M}}}{dt} = \bar{\bar{n}} t_*, \quad (9)$$

where $\bar{\bar{n}}$ is the dimensional mean motion for the spacecraft (satellite) around the Moon supplied with $\bar{\bar{a}}$.

2.3 Circular Restricted Three-Body Problem (CR3BP)

The CR3BP dynamics are cast within the BRF. The equations of motion are rendered as [2],

$$\ddot{\vec{\rho}} = -2\hat{z} \times \dot{\vec{\rho}} + \nabla V. \quad (10)$$

The double prime indicates a second derivative with respect to the nd time, t . The vector cross product is denoted as \times , and V is the pseudo-potential function rendered as $V = 1/2 \cdot (x^2 + y^2) + (1 - \mu)/d + \mu/r$ where d and r correspond to the nd distance between the spacecraft and Earth, and the spacecraft and Moon, respectively.

2.4 Higher-Fidelity Ephemeris Model (HFEM)

The higher-fidelity modeling in the current investigation includes point-mass gravity from three celestial bodies: the Sun (S), Earth (E), and Moon (M). The instantaneous locations of the bodies are retrieved from the JPL ephemerides DE440 [34]. With the Moon as the central gravitational body, the equations of motion for the spacecraft within the JIF are rendered,

$$\ddot{\vec{R}} = -\frac{\mu}{R^3} \vec{R} + \sum_{j=E,S} \left[\frac{\mu_j}{R_{jM}^3} \vec{R}_{jM} - \frac{\mu_j}{R_{jc}^3} \vec{R}_{jc} \right], \quad (11)$$

where \vec{R}_{jc} and \vec{R}_{jM} denote the nd position vectors from the perturbing body j to the spacecraft and the Moon, respectively. The nd gravitational parameter μ_j is defined as $\mu_j = \tilde{\mu}_j / (\tilde{\mu}_E + \tilde{\mu}_M)$. Subscripts E, S are leveraged to indicate the Earth and the Sun, respectively.

2.5 Quasi-Periodic Orbits (QPOs) and Frequency Decomposition

Quasi-Periodic Orbits (QPOs) arise naturally in the models incorporated throughout this investigation, but their characteristics depend on the underlying dynamical system. The Doubly-Averaged Dynamical Model (DADM) is an integrable Hamiltonian system with three degrees of freedom and three integrals of motion. All solutions exhibit (quasi-)periodic behavior. The Circular Restricted Three-Body Problem (CR3BP), while non-integrable, retains one integral of motion in the BRF and admits quasi-periodic solutions within certain regimes. Both models are time-independent and supply QPOs with the maximum dimension of $n_i = 3$. Due to the low dimensional complexity, existing strategies such as GMOS are suitable for construction of QPOs for these simplified models. In contrast, the Higher-Fidelity Ephemeris Model (HFEM) introduces additional time-dependent perturbations, generally increasing the number of fundamental frequencies from n_i to $n = n_i + n_e$. Under resonant interactions, $n = n_i + n_e - 1$. This work focuses on dynamical regimes where the QPOs persist and analog structures are well-defined within the HFEM. Each QPO is characterized by n fundamental frequencies. The full state vector on the QPO evolves as an infinite Fourier series comprised of linear combinations of these frequencies. Accurate recovery of these frequency components is central to the corrections strategy developed in this work.

3 Frequency Refinement Methods

While the existence of Quasi-Periodic Orbits (QPOs) analytically guarantees that a trajectory on such a torus is represented as a Fourier series, numerically reconstructing this structure poses significant challenges. Since these trajectories are not available in closed form but are instead generated through sequential numerical integration, the Discrete Fourier Transform (DFT) is employed in place of the Continuous Fourier Transform (CFT). However, the inherent limitations of the DFT hinder accurate frequency recovery. These challenges include, but are not limited to, spectral leakage, limited frequency resolution, and aliasing from components above the Nyquist threshold [37].

To supply accurate frequency structures associated with quasi-periodic trajectories, the information from the DFT is *refined*. To formalize the frequency refinement process, a scalar signal $q(t)$ is sampled along a quasi-periodic trajectory γ . Typical choices for q include position or velocity components, distances

to primary bodies, or angular quantities relative to a reference direction. The objective is to construct a quasi-periodic approximation $\tilde{q}(t)$ of the form,

$$q(t) \approx \tilde{q}(t) = A_0 + \sum_{j=1}^m A_j \cos(\mathbf{f}_j t + \theta_j) = A_0 + \sum_{j=1}^m \tilde{q}_j(t), \quad (12)$$

where A_j , \mathbf{f}_j , and θ_j represent the amplitude, frequency, and phase of the j -th quasi-periodic component. The number of terms m is user-defined. Due to the discrete nature of the DFT, however, the identified peaks generally do not align exactly with the true frequency components \mathbf{f}_j . Consequently, the corresponding amplitude and phase estimates from the DFT are often insufficient, necessitating a refinement process. The quantities to be refined at each step are collected as,

$$\vec{\xi}_j = \begin{bmatrix} \mathbf{f}_j \\ A_j \\ \theta_j \end{bmatrix}. \quad (13)$$

Two frequency refinement strategies are employed to estimate $\vec{\xi}$: (i) Laskar-Numerical Analysis of Fundamental Frequency (L-NAFF) method [27] and (ii) Gómez-Mondelo-Simó-Collocation (GMS-C) method [28]. Both methods define a set of algebraic constraints, and a differential corrections process is used to iteratively refine $\vec{\xi}$ to satisfy these conditions. The notation introduced below largely follows the formulation in [28]. First, consider DFT on a quasi-periodic trajectory, γ . The time-domain signal is constructed as,

$$q(t_i), \quad (0 \leq i \leq N-1) \quad (14)$$

$$t_i = \Delta t i \quad (15)$$

$$T = \Delta t N, \quad (16)$$

where Δt is the sample spacing and T is the total time span. The sample size is denoted as N . The Discrete Fourier Transform (DFT) of q is defined as,

$$\mathcal{D}_q(f) := \frac{1}{N} \sum_{i=0}^{N-1} q(t_i) h(i) e^{-\mathbf{i} f t_i}, \quad (17)$$

where f is a general notation for a frequency. The frequencies in the current analysis are represented in the units of radians per respective unit time (not to be confused with cycles per unit time). The Hann window function of order two, i.e., $h(i) = 2/3(1 - \cos(2\pi i/N))^2$, is applied to alleviate spectral leakage [37]. While T and N serve as parameters for the DFT in Eq. (17), they are assumed to be arbitrarily fixed numbers for notational brevity. In the *standard* DFT, frequency bins are defined at $(N/2 + 1)$ equally spaced points, corresponding to,

$$\Delta\omega = \frac{2\pi}{T} \quad (18)$$

$$\omega_k = \Delta\omega k = \frac{2\pi k}{T}, \quad (0 \leq k \leq N/2), \quad (19)$$

where N is assumed to be even (as is typical when using an Fast Fourier Transform (FFT)). The bin width $\Delta\omega$ is solely a function of T , where generally, investigating signals over a longer horizon time results in enhanced frequency resolutions. Evaluating the DFT at bin ω_k yields,

$$\mathcal{D}_q(\omega_k) = \frac{1}{N} \sum_{i=0}^{N-1} q(t_i) h(i) e^{\frac{-2\pi \mathbf{i} i k}{N}} = \frac{1}{N} \sum_{i=0}^{N-1} q(t_i) h(i) e^{-\mathbf{i} \omega_k t_i} \quad (20)$$

$$= \frac{1}{N} \sum_{i=0}^{N-1} \left(q(t_i) h(i) (\cos(\omega_k t_i) - \mathbf{i} \sin(\omega_k t_i)) \right). \quad (21)$$

The imaginary number is denoted as \mathbf{i} , i.e., $\mathbf{i}^2 = -1$. Now, define the following quantities,

$$\mathcal{C}_q(\omega_k) = 2\text{Re}(\mathcal{D}_q(\omega_k)) \quad (22)$$

$$\mathcal{S}_q(\omega_k) = -2\text{Im}(\mathcal{D}_q(\omega_k)), \quad (23)$$

connected to the cosine (real) and sine (imag) components of $\mathcal{D}_q(\omega_k)$. From the standard DFT analysis on the signal from Eq. (20), *peaks* emerge that satisfy,

$$|\mathcal{D}_q(\omega_k)| \geq |\mathcal{D}_q(\omega_{k-1})| \quad \text{and} \quad |\mathcal{D}_q(\omega_k)| \geq |\mathcal{D}_q(\omega_{k+1})|. \quad (24)$$

For a quasi-periodic signal q , prominent peaks typically emerge in the vicinity of the true frequency components. The j -th peak from the bin frequency (Eq.(20)) is denoted as,

$$\omega_k^{*j}, \quad (25)$$

and,

$$\omega_{k\pm 1}^{*j} = \omega_k^{*j} \pm \Delta\omega, \quad (26)$$

corresponding to the adjacent bins to ω_k . The initial guess for the free variables (Eq. (13)) associated with the j -th peak is supplied from the DFT as,

$$\mathbf{f}_j \approx \omega_k^{*j} \quad (27)$$

$$A_j \approx 2|\mathcal{D}_q(\omega_k^{*j})| = \sqrt{(\mathcal{C}_q(\omega_k^{*j}))^2 + (\mathcal{S}_q(\omega_k^{*j}))^2} \quad (28)$$

$$\theta_j \approx \arctan_2(-\mathcal{S}_q(\omega_k^{*j}), \mathcal{C}_q(\omega_k^{*j})), \quad (29)$$

where \arctan_2 is the four-quadrant inverse tangent. Alternatively, an optimization problem may be formulated to locate $\tilde{q}_j = A_j \cos(\mathbf{f}_j t + \theta_j)$ from Eq. (12) that minimizes the error $e = \sum_{i=0}^{N-1} (q(t_i) - \tilde{q}_j(t_i))^2$. The initial guess is subsequently refined using either the Laskar-Numerical Analysis of Fundamental Frequency (L-NAFF) or Gómez-Mondelo-Simó-Collocation (GMS-C) methods that are described in the following sections. In both methods, the quasi-periodic representation \tilde{q} (Eq. (12)) is sequentially refined for $j \leq m$.

3.1 Laskar-Numerical Analysis of Fundamental Frequency (L-NAFF) Method [27]

At the j -th step, the L-NAFF method seeks to refine the frequency estimate \mathbf{f}_j such that the magnitude of the DFT for the signal q is maximized at this frequency. This refinement condition is defined as,

$$\mathbf{f}_j = \arg \max_{\mathbf{f}} |\mathcal{D}_q(\mathbf{f})|. \quad (30)$$

The *auxiliary* DFT, $\mathcal{D}_q(\mathbf{f})$, is the continuous-frequency DFT of q , constructed as,

$$\mathcal{D}_q(\mathbf{f}) = \frac{1}{N} \sum_{i=0}^{N-1} q(t_i) h(i) e^{-\mathbf{i}\mathbf{f}t_i} \quad (31)$$

$$= \frac{1}{N} \sum_{i=0}^{N-1} q(t_i) h(i) [\cos(\mathbf{f}t_i) - \mathbf{i} \sin(\mathbf{f}t_i)]. \quad (32)$$

Note that \mathbf{f} represents a continuous frequency and may differ from the discretized frequency bins ω_k defined in the standard DFT. The magnitude of $\mathcal{D}_q(\mathbf{f})$ is expressed as,

$$|\mathcal{D}_q(\mathbf{f})| = \frac{1}{2} \sqrt{\mathcal{C}_q(\mathbf{f})^2 + \mathcal{S}_q(\mathbf{f})^2}, \quad (33)$$

where the real and imaginary components are defined as,

$$\mathcal{C}_q(\mathbf{f}) = \frac{2}{N} \sum_{i=0}^{N-1} q(t_i) h(i) \cos(\mathbf{f}t_i), \quad (34)$$

$$\mathcal{S}_q(\mathbf{f}) = \frac{2}{N} \sum_{i=0}^{N-1} q(t_i) h(i) \sin(\mathbf{f}t_i). \quad (35)$$

Then, at the maximum frequency from Eq. (30), following first derivative results in zero,

$$\text{L-NAFF Constraint 1} \quad \frac{d}{d\mathbf{f}_j} |\mathcal{D}_q(\mathbf{f}_j)| = \frac{1}{2\sqrt{\mathcal{C}_q^2 + \mathcal{S}_q^2}} \left(\mathcal{C}_q \frac{d\mathcal{C}_q}{d\mathbf{f}_j} + \mathcal{S}_q \frac{d\mathcal{S}_q}{d\mathbf{f}_j} \right) = 0. \quad (36)$$

The derivatives of the cosine and sine components are,

$$\frac{d\mathcal{C}_q}{d\mathbf{f}_j} = -\frac{2}{N} \sum_{i=0}^{N-1} t_i q(t_i) h(i) \sin(\mathbf{f}_j t_i), \quad (37)$$

$$\frac{d\mathcal{S}_q}{d\mathbf{f}_j} = \frac{2}{N} \sum_{i=0}^{N-1} t_i q(t_i) h(i) \cos(\mathbf{f}_j t_i). \quad (38)$$

To refine the amplitude A_j and phase θ_j , the j -th approximated signal from Eq. (12), i.e.,

$$\tilde{q}_j(t) = A_j \cos(\mathbf{f}_j t + \theta_j), \quad (39)$$

is leveraged. The DFT on $\tilde{q}_j(t)$ is required to match that of the original signal, i.e.,

$$\mathcal{D}_{\tilde{q}_j}(\mathbf{f}_j) = \mathcal{D}_q(\mathbf{f}_j). \quad (40)$$

Writing \tilde{q}_j as $\tilde{q}_j(t) = A_j \cos \theta_j \cos(\mathbf{f}_j t) - A_j \sin \theta_j \sin(\mathbf{f}_j t)$ and applying the DFT yields,

$$\begin{aligned} \mathcal{D}_{\tilde{q}_j}(\mathbf{f}_j) &= \frac{1}{2} \left[A_j \cos \theta_j \mathcal{C}_{c(\mathbf{f}_j)}(\mathbf{f}_j) - A_j \sin \theta_j \mathcal{C}_{s(\mathbf{f}_j)}(\mathbf{f}_j) \right] \\ &\quad + \frac{j}{2} \left[-A_j \cos \theta_j \mathcal{S}_{c(\mathbf{f}_j)}(\mathbf{f}_j) + A_j \sin \theta_j \mathcal{S}_{s(\mathbf{f}_j)}(\mathbf{f}_j) \right], \end{aligned} \quad (41)$$

where each auxiliary quantity is defined as:

$$\mathcal{C}_{c(\mathbf{f}_j)}(\mathbf{f}_j) = \frac{2}{N} \sum_{i=0}^{N-1} \cos^2(\mathbf{f}_j t_i) h(i) \approx 1, \quad (42)$$

$$\mathcal{C}_{s(\mathbf{f}_j)}(\mathbf{f}_j) = \frac{2}{N} \sum_{i=0}^{N-1} \cos(\mathbf{f}_j t_i) \sin(\mathbf{f}_j t_i) h(i) \approx 0, \quad (43)$$

$$\mathcal{S}_{c(\mathbf{f}_j)}(\mathbf{f}_j) = \mathcal{C}_{s(\mathbf{f}_j)}(\mathbf{f}_j), \quad (44)$$

$$\mathcal{S}_{s(\mathbf{f}_j)}(\mathbf{f}_j) = \frac{2}{N} \sum_{i=0}^{N-1} \sin^2(\mathbf{f}_j t_i) h(i) \approx 1. \quad (45)$$

Matching the real and imaginary parts yields two additional constraints,

$$\text{L-NAFF Constraint 2} \quad A_j \cos \theta_j \mathcal{C}_{c(\mathbf{f}_j)}(\mathbf{f}_j) - A_j \sin \theta_j \mathcal{C}_{s(\mathbf{f}_j)}(\mathbf{f}_j) = \mathcal{C}_q, \quad (46)$$

$$\text{L-NAFF Constraint 3} \quad A_j \cos \theta_j \mathcal{S}_{c(\mathbf{f}_j)}(\mathbf{f}_j) - A_j \sin \theta_j \mathcal{S}_{s(\mathbf{f}_j)}(\mathbf{f}_j) = \mathcal{S}_q. \quad (47)$$

Together, Eqs. (36), (46), (47) define the constraint vector for L-NAFF as,

$$\vec{F}_{L,j} = \begin{bmatrix} F_{L,\mathbf{f}} \\ F_{L,\mathcal{C}} \\ F_{L,\mathcal{S}} \end{bmatrix} = \begin{bmatrix} \frac{1}{2\sqrt{\mathcal{C}_q(\mathbf{f}_j)^2 + \mathcal{S}_q(\mathbf{f}_j)^2}} \left(\mathcal{C}_q(\mathbf{f}_j) \frac{d\mathcal{C}_q(\mathbf{f}_j)}{d\mathbf{f}_j} + \mathcal{S}_q(\mathbf{f}_j) \frac{d\mathcal{S}_q(\mathbf{f}_j)}{d\mathbf{f}_j} \right) \\ A_j \cos \theta_j \mathcal{C}_{c(\mathbf{f}_j)}(\mathbf{f}_j) - A_j \sin \theta_j \mathcal{C}_{s(\mathbf{f}_j)}(\mathbf{f}_j) - \mathcal{C}_q(\mathbf{f}_j) \\ A_j \cos \theta_j \mathcal{S}_{c(\mathbf{f}_j)}(\mathbf{f}_j) - A_j \sin \theta_j \mathcal{S}_{s(\mathbf{f}_j)}(\mathbf{f}_j) - \mathcal{S}_q(\mathbf{f}_j) \end{bmatrix} = \vec{0}, \quad (48)$$

solved via differential corrections. The Jacobian matrix of $\vec{F}_{L,j}$ with respect to $\vec{\xi}_j$ renders,

$$\frac{\partial \vec{F}_{L,j}}{\partial \vec{\xi}_j} = \begin{bmatrix} \frac{\partial F_{L,\mathbf{f}}}{\partial \mathbf{f}_j} & \frac{\partial F_{L,\mathbf{f}}}{\partial A_j} & \frac{\partial F_{L,\mathbf{f}}}{\partial \theta_j} \\ \frac{\partial F_{L,\mathcal{C}}}{\partial \mathbf{f}_j} & \frac{\partial F_{L,\mathcal{C}}}{\partial A_j} & \frac{\partial F_{L,\mathcal{C}}}{\partial \theta_j} \\ \frac{\partial F_{L,\mathcal{S}}}{\partial \mathbf{f}_j} & \frac{\partial F_{L,\mathcal{S}}}{\partial A_j} & \frac{\partial F_{L,\mathcal{S}}}{\partial \theta_j} \end{bmatrix}, \quad (49)$$

with each component derived analytically using the chain rule and second derivatives of \mathcal{C}_q and \mathcal{S}_q , included in Appendix A. After convergence of the j -th frequency component, the next peak ($j + 1$) is detected from the residual signal,

$$q_j^{new} := q - (A_0 + \sum_{a=1}^j \tilde{q}_a) \quad (50)$$

In the new signal q_j^{new} , the $(j + 1)$ -th peak from the original signal q is expected to occur as the most dominant peak, facilitating the isolation of subsequent lower-amplitude components. The zeroth-order term A_0 is trivially constructed as the average of q .

3.2 Gómez-Mondelo-Simó-Collocation (GMS-C) Method [28]

In contrast to the L-NAFF method that directly maximizes the DFT magnitude at the approximated frequency, the GMS-C approach refines the frequency estimate \mathbf{f}_j by enforcing collocation conditions in adjacent frequency bins. This strategy relies on matching the DFT of the approximated signal \tilde{q}_j to that of the original signal q at these selected frequencies. To formulate the algebraic constraints, consider the DFTs of cosine and sine functions evaluated at ω_k , the k -th bin from the *standard* DFT,

$$\mathcal{D}_{c(\mathbf{f}_j)}(\omega_k) = \frac{1}{N} \sum_{i=0}^{N-1} \cos(\mathbf{f}_j t_i) h(i) e^{-i\omega_k t_i}, \quad (51)$$

$$\mathcal{D}_{s(\mathbf{f}_j)}(\omega_k) = \frac{1}{N} \sum_{i=0}^{N-1} \sin(\mathbf{f}_j t_i) h(i) e^{-i\omega_k t_i}, \quad (52)$$

$$\frac{d\mathcal{D}_{c(\mathbf{f}_j)}(\omega_k)}{d\mathbf{f}_j} = -\frac{1}{N} \sum_{i=0}^{N-1} t_i \sin(\mathbf{f}_j t_i) h(i) e^{-i\omega_k t_i}, \quad (53)$$

$$\frac{d\mathcal{D}_{s(\mathbf{f}_j)}(\omega_k)}{d\mathbf{f}_j} = \frac{1}{N} \sum_{i=0}^{N-1} t_i \cos(\mathbf{f}_j t_i) h(i) e^{-i\omega_k t_i}. \quad (54)$$

The following real-valued quantities are defined for use in the constraint expressions,

$$\mathcal{C}_{c(\mathbf{f}_j)}(\omega_k) = 2 \operatorname{Re}(\mathcal{D}_{c(\mathbf{f}_j)}(\omega_k)), \quad \mathcal{C}_{s(\mathbf{f}_j)}(\omega_k) = 2 \operatorname{Re}(\mathcal{D}_{s(\mathbf{f}_j)}(\omega_k)), \quad (55)$$

$$\mathcal{S}_{c(\mathbf{f}_j)}(\omega_k) = -2 \operatorname{Im}(\mathcal{D}_{c(\mathbf{f}_j)}(\omega_k)), \quad \mathcal{S}_{s(\mathbf{f}_j)}(\omega_k) = -2 \operatorname{Im}(\mathcal{D}_{s(\mathbf{f}_j)}(\omega_k)), \quad (56)$$

$$\frac{d\mathcal{C}_{c(\mathbf{f}_j)}(\omega_k)}{d\mathbf{f}_j} = 2 \operatorname{Re} \left(\frac{d\mathcal{D}_{c(\mathbf{f}_j)}(\omega_k)}{d\mathbf{f}_j} \right), \quad \frac{d\mathcal{C}_{s(\mathbf{f}_j)}(\omega_k)}{d\mathbf{f}_j} = 2 \operatorname{Re} \left(\frac{d\mathcal{D}_{s(\mathbf{f}_j)}(\omega_k)}{d\mathbf{f}_j} \right), \quad (57)$$

$$\frac{d\mathcal{S}_{c(\mathbf{f}_j)}(\omega_k)}{d\mathbf{f}_j} = -2 \operatorname{Im} \left(\frac{d\mathcal{D}_{c(\mathbf{f}_j)}(\omega_k)}{d\mathbf{f}_j} \right), \quad \frac{d\mathcal{S}_{s(\mathbf{f}_j)}(\omega_k)}{d\mathbf{f}_j} = -2 \operatorname{Im} \left(\frac{d\mathcal{D}_{s(\mathbf{f}_j)}(\omega_k)}{d\mathbf{f}_j} \right). \quad (58)$$

Based on this auxiliary DFT information, the GMS-C refinement process enforces collocation at two frequencies: (1) the j -th DFT peak, ω_k^{*j} , and (2) one of its adjacent bins, $\omega_{k\pm 1}^{*j}$ from Eq. (26). Equivalently,

$$\mathcal{D}_{\tilde{q}_j}(\omega_k^{*j}) = \mathcal{D}_q(\omega_k^{*j}), \quad (59)$$

$$\mathcal{D}_{\tilde{q}_j}(\omega_{k\pm 1}^{*j}) = \mathcal{D}_q(\omega_{k\pm 1}^{*j}). \quad (60)$$

The auxiliary frequency $\omega_{k\pm 1}^{*j}$ is selected from ω_{k-1}^{*j} and ω_{k+1}^{*j} based on the larger DFT amplitude of the original signal. Specifically, $\omega_{k\pm 1}^{*j}$ corresponds to the neighboring bin that yields the greater value of $|\mathcal{D}_q(\omega_{k\pm 1}^{*j})|$. Since each DFT match from Eqs. (59)-(60) introduces two scalar conditions (real and imaginary parts), these constraints overdetermine the three-element state vector $\vec{\xi}_j$ from Eq. (13). To ensure an invertible

Jacobian, only one component (cosine or sine) is enforced at $\omega_{k\pm 1}^{*j}$, selected based on conditioning [38]. The resulting three scalar constraints are:

$$\text{GMS-C Constraint 1} \quad A_j \cos \theta_j \mathcal{C}_{c(\mathbf{f}_j)}(\omega_k^{*j}) - A_j \sin \theta_j \mathcal{C}_{s(\mathbf{f}_j)}(\omega_k^{*j}) = \mathcal{C}_q(\omega_k^{*j}), \quad (61)$$

$$\text{GMS-C Constraint 2} \quad A_j \cos \theta_j \mathcal{S}_{c(\mathbf{f}_j)}(\omega_k^{*j}) - A_j \sin \theta_j \mathcal{S}_{s(\mathbf{f}_j)}(\omega_k^{*j}) = \mathcal{S}_q(\omega_k^{*j}), \quad (62)$$

$$\text{GMS-C Constraint 3} \quad A_j \cos \theta_j \mathcal{CS}_{c(\mathbf{f}_j)}(\omega_{k\pm 1}^{*j}) - A_j \sin \theta_j \mathcal{CS}_{s(\mathbf{f}_j)}(\omega_{k\pm 1}^{*j}) = \mathcal{CS}_q(\omega_{k\pm 1}^{*j}), \quad (63)$$

where \mathcal{CS} denotes that one of the \mathcal{C} or \mathcal{S} is selected based on the condition from Appendix A. Three collocation conditions (Eqs. (61)-(63)) are concatenated as,

$$\vec{F}_{G,j} = \begin{bmatrix} F_{G,\mathcal{C}(\omega_k^{*j})} \\ F_{G,\mathcal{S}(\omega_k^{*j})} \\ F_{G,\mathcal{CS}(\omega_{k\pm 1}^{*j})} \end{bmatrix} = \begin{bmatrix} A_j \cos \theta_j \mathcal{C}_{c(\mathbf{f}_j)}(\omega_k^{*j}) - A_j \sin \theta_j \mathcal{C}_{s(\mathbf{f}_j)}(\omega_k^{*j}) - \mathcal{C}_q(\omega_k^{*j}) \\ A_j \cos \theta_j \mathcal{S}_{c(\mathbf{f}_j)}(\omega_k^{*j}) - A_j \sin \theta_j \mathcal{S}_{s(\mathbf{f}_j)}(\omega_k^{*j}) - \mathcal{S}_q(\omega_k^{*j}) \\ A_j \cos \theta_j \mathcal{CS}_{c(\mathbf{f}_j)}(\omega_{k\pm 1}^{*j}) - A_j \sin \theta_j \mathcal{CS}_{s(\mathbf{f}_j)}(\omega_{k\pm 1}^{*j}) - \mathcal{CS}_q(\omega_{k\pm 1}^{*j}) \end{bmatrix} = \vec{0}. \quad (64)$$

The Jacobian $\partial \vec{F}_{G,j} / \partial \vec{\xi}$ is constructed as follows,

$$\frac{\partial \vec{F}_{G,j}}{\partial \vec{\xi}_j} = \begin{bmatrix} \frac{\partial F_{G,\mathcal{C}(\omega_k^{*j})}}{\partial \mathbf{f}_j} & \frac{\partial F_{G,\mathcal{C}(\omega_k^{*j})}}{\partial A_j} & \frac{\partial F_{G,\mathcal{C}(\omega_k^{*j})}}{\partial \theta_j} \\ \frac{\partial F_{G,\mathcal{S}(\omega_k^{*j})}}{\partial \mathbf{f}_j} & \frac{\partial F_{G,\mathcal{S}(\omega_k^{*j})}}{\partial A_j} & \frac{\partial F_{G,\mathcal{S}(\omega_k^{*j})}}{\partial \theta_j} \\ \frac{\partial F_{G,\mathcal{CS}(\omega_{k\pm 1}^{*j})}}{\partial \mathbf{f}_j} & \frac{\partial F_{G,\mathcal{CS}(\omega_{k\pm 1}^{*j})}}{\partial A_j} & \frac{\partial F_{G,\mathcal{CS}(\omega_{k\pm 1}^{*j})}}{\partial \theta_j} \end{bmatrix}, \quad (65)$$

where each component is supplied in Appendix A.

3.3 Numerical Comparison of the Two Refinement Strategies

The two refinement strategies, L-NAFF and GMS-C, share a common goal to refine quasi-periodic approximations with auxiliary DFT-based constraints. The auxiliary DFTs yield algebraic conditions (Eqs. (48) and (64)) that are enforced by adjusting the free-variable vector (Eq. (13)). Recall that the *standard* DFT refers to the signal transform in Eq. (17) evaluated at the discrete frequency bins (Eq. (19)). The two refinement methods differ then as follows: (1) L-NAFF applies the DFT directly to q , but at continuous frequencies \mathbf{f}_j that generally do not align with the bin centers (i.e., $\mathbf{f}_j \neq \omega_k$), and (2) GMS-C instead evaluates the DFT at the standard bins, but on a cosine and sine basis signals defined by \mathbf{f}_j . Another distinction emerges when examining the Jacobian matrices in Eqs. (49) and (65). In the L-NAFF strategy, the constraint vector at the j -th step depends only on the corresponding free-variable vector $\vec{\xi}_j$. In contrast, the GMS-C method introduces interdependencies across modes: the Jacobian $\partial \vec{F}_l / \partial \vec{\xi}_j$ is generally nonzero for all $l \neq j$. As a result, the GMS-C strategy refines the first j frequency components simultaneously at the j -th step. Moreover, the zeroth-order coefficient A_0 is also subject to refinement in the GMS-C formulation. While this aspect is not directly leveraged in the current investigation, further details are found in Gómez, Mondelo, and Simó [28].

To illustrate the difference in performance between these two strategies, consider a sample CR3BP Distant Retrograde Orbit (DRO) as illustrated in Fig. 2. The initial condition for the orbit is supplied in Table 1. Along the periodic orbit, $N = 2^{16}$ samples on the x -position components are constructed and leveraged as q for the DFT over 20 years. Note that the period of the DRO is 1.6 (nd), where the fundamental frequency corresponds to $\nu_C = 2\pi/1.6 \approx 3.927$ (nd). The resulting DFT spectrum is included in Fig. 3, with dot markers at each frequency bin. The vertical axis illustrates \log_{10} of the DFT amplitude (A). While the peaks are generally associated with multiples of ν_C , due to the aforementioned limitations in the DFT, refinement strategies are employed. The results are illustrated in red and blue within Fig. 3 for the L-NAFF and Gómez-Mondelo-Simó-Collocation (GMS-C) methods, respectively. Figure 4 illustrates the frequency errors (in comparison to integer multiples of ν_C) after applying each refinement. No marker appears for ν_C (multiple 1), as both methods resolve it to near-zero error. While the detailed performance varies depending on factors like numerical formulation and sampling resolution, **both methods supply accurate estimates for the dominant peaks within the lower-frequency domain**. Throughout the current investigation, both strategies are leveraged interchangeably.

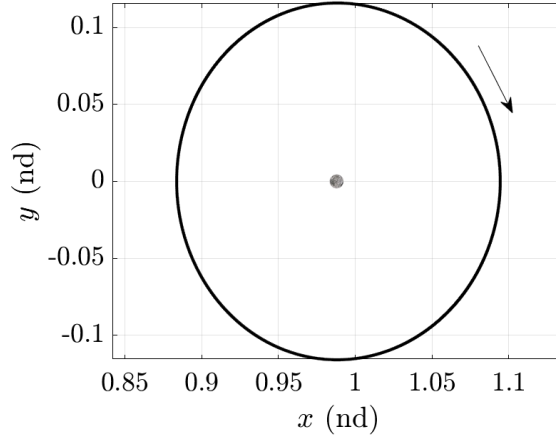


Fig. 2: Sample CR3BP periodic-DRO within the Barycentric Rotating Frame (BRF)

Table 1: Period and initial state for the periodic-DRO represented in Fig. 2

Variable	Value (nd)
period	1.6
x	0.883749964899239
y	0
z	0
x'	0
y'	0.470425740470053
z'	0

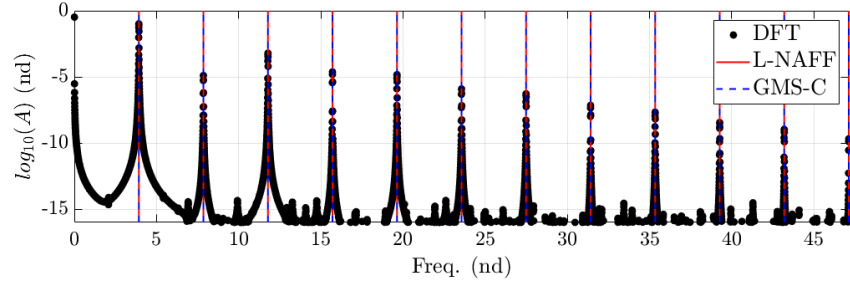


Fig. 3: DFT on x -position components for the periodic-DRO in Fig. 2

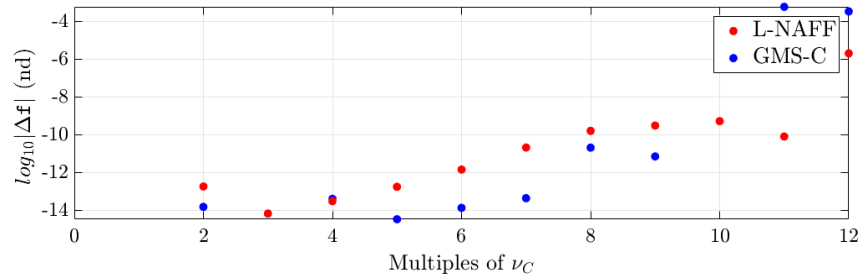


Fig. 4: Errors for refined frequencies at the multiples of ν_C

4 Frequency-Domain Differential Corrector (FDDC): Single-Shooting Formulation

The overarching goal of this investigation is to develop a Frequency-Domain Differential Corrector (FDDC) capable of generating n -dimensional Quasi-Periodic Orbits (QPOs). The preceding section introduces two refinement strategies that, given a fixed signal q , extract accurate representations of individual frequency components, i.e., \mathbf{f}_j , A_j , and θ_j , associated with the j -th peak in the frequency-domain. In contrast, the FDDC adjusts the signal itself so that these spectral components match desired target values, thereby controlling the underlying n -dimensional QPO.

This section (single-shooting formulation) focuses on dynamical regimes that are locally stable, i.e., those free of strong instabilities. In such settings, the signal q is supplied by propagating a single six-dimensional initial state $\vec{\mathbb{X}}_0 \in \mathbb{R}^6$ over a long time-span. To establish the core algorithm, a generic, autonomous n_i degree-of-freedom Hamiltonian system is examined as the governing dynamics. Within such systems, dynamical regimes may exist where dense n_i -dimensional QPOs exist locally, demonstrating a stable behavior.¹ Relevant examples in the Earth–Moon CR3BP include, but are not limited to, the Distant Retrograde Orbit (DRO) family and the Elliptical Lunar Frozen Orbits (ELFOs). The single-shooting FDDC formulation assumes the initial state $\vec{\mathbb{X}}_0$ as the free variable and enforces the following constraint,

$$\vec{\mathbb{F}}_f = \begin{bmatrix} \mathbf{f}_j - \mathbf{f}_j^T \\ \theta_j - \theta_j^T \end{bmatrix} \quad \text{or} \quad \begin{bmatrix} A_j - A_j^T \\ \theta_j - \theta_j^T \end{bmatrix}, \quad (66)$$

where the superscript T denotes the target frequency-domain quantities. Importantly, the amplitude and frequency components A_j and \mathbf{f}_j are generally coupled within a QPO. Attempting to target both simultaneously typically results in an over-constrained system. Therefore, the FDDC formulation targets either \mathbf{f}_j or A_j , depending on the application. To construct a differential corrector, the gradient of $\vec{\mathbb{F}}_f$ with respect to $\vec{\mathbb{X}}_0$ is required. Specifically, the following sensitivities must be supplied,

$$\frac{\partial \mathbf{f}_j}{\partial \vec{\mathbb{X}}_0}, \quad \frac{\partial A_j}{\partial \vec{\mathbb{X}}_0}, \quad \frac{\partial \theta_j}{\partial \vec{\mathbb{X}}_0}. \quad (67)$$

These derivatives are constructed by differentiating the algebraic constraints associated with the refinement strategies introduced from Eqs. (48) and (64). The required sensitivity expressions for each method are presented in the following subsections.

4.1 Sensitivities of the State Vector on the Frequency Components

The sensitivities of \mathbf{f}_j , A_j , and θ_j with respect to the initial state $\vec{\mathbb{X}}_0$ are derived for both refinement methods. This section focuses on the single-shooting formulation, where the signal q is generated by forward propagation of $\vec{\mathbb{X}}_0$ under any dynamical model. Note that,

$$\vec{\mathbf{X}}^{t_i}(\vec{\mathbb{X}}_0; \mathbf{t}_0) \quad (68)$$

denotes the state propagated from $\vec{\mathbb{X}}_0$ initiating at the epoch \mathbf{t}_0 (assumed to be fixed), propagated for t_i . Then, the sensitivity of the propagated state as the initial state evolves is captured by the State Transition Matrix (STM). The STM from the initial state $\vec{\mathbb{X}}_0$ at epoch t_0 to time t_i is denoted $\phi^{t_i}(\vec{\mathbb{X}}_0; \mathbf{t}_0)$, and satisfies,

$$\frac{d\vec{\mathbf{X}}^{t_i}(\vec{\mathbb{X}}_0; \mathbf{t}_0)}{d\vec{\mathbb{X}}_0} = \phi^{t_i}(\vec{\mathbb{X}}_0; \mathbf{t}_0). \quad (69)$$

The sensitivity of any scalar signal $q(t_i)$ derived from the state vector is produced through the chain rule,

$$\frac{dq(t_i)}{d\vec{\mathbb{X}}_0} = \frac{dq(t_i)}{d\vec{\mathbf{X}}^{t_i}(\vec{\mathbb{X}}_0; \mathbf{t}_0)} \cdot \phi^{t_i}(\vec{\mathbb{X}}_0; \mathbf{t}_0). \quad (70)$$

Depending on the model and the frame, q may or may not correspond trivially to a state component from $\vec{\mathbf{X}}$, illustrated further in the subsequent numerical examples.

¹Although resonant periodic orbits in the vicinity of the dense n_i -dimensional QPOs with $n_i > 2$ may introduce weak instabilities due to Arnold diffusion [1], their growth rates are super-exponentially slow [39].

4.1.1 Sensitivities within the Laskar-Numerical Analysis of Fundamental Frequency (L-NAFF) Method

The sensitivities in Eq. (67) are characterized via differentiating the constraint vector from the L-NAFF method, i.e., Eq. (48). The process yields,

$$\frac{\partial \vec{F}_{L,j}}{\partial \vec{\xi}_j} \begin{bmatrix} \frac{\partial \mathbf{f}_j}{\partial \vec{x}_0} \\ \frac{\partial A_j}{\partial \vec{x}_0} \\ \frac{\partial \theta_j}{\partial \vec{x}_0} \end{bmatrix} = - \begin{bmatrix} \frac{\partial F_{L,f}}{\partial \vec{x}_0} \\ \frac{\partial F_{L,c}}{\partial \vec{x}_0} \\ \frac{\partial F_{L,s}}{\partial \vec{x}_0} \end{bmatrix}. \quad (71)$$

The first term, $\frac{\partial \vec{F}_{L,j}}{\partial \vec{\xi}_j}$, is an invertible matrix constructed from Eq. (49). The vector components on the right side of Eq. (71) involve expressions from Eq. (70) and are supplied in Appendix B. Then, it is possible to invert the matrix and write,

$$\begin{bmatrix} \frac{\partial \mathbf{f}_j}{\partial \vec{x}_0} \\ \frac{\partial A_j}{\partial \vec{x}_0} \\ \frac{\partial \theta_j}{\partial \vec{x}_0} \end{bmatrix} = - \left(\frac{\partial \vec{F}_{L,j}}{\partial \vec{\xi}_j} \right)^{-1} \begin{bmatrix} \frac{\partial F_{L,f}}{\partial \vec{x}_0} \\ \frac{\partial F_{L,c}}{\partial \vec{x}_0} \\ \frac{\partial F_{L,s}}{\partial \vec{x}_0} \end{bmatrix}, \quad (72)$$

supplying the sensitivities in Eq. (67). Note that the left side of Eq. (72) is a (3×6) matrix.

4.1.2 Sensitivities within the Gómez-Mondelo-Simó-Collocation (GMS-C) Method

A similar process is now initiated with the GMS-C method. Differentiating Eq. (64) yields,

$$\frac{\partial \vec{F}_{G,j}}{\partial \vec{\xi}} \begin{bmatrix} \frac{\partial \mathbf{f}_j}{\partial \vec{x}_0} \\ \frac{\partial A_j}{\partial \vec{x}_0} \\ \frac{\partial \theta_j}{\partial \vec{x}_0} \end{bmatrix} = - \begin{bmatrix} \frac{\partial F_{G,C(\omega_k^{*j})}}{\partial \vec{x}_0} \\ \frac{\partial F_{G,S(\omega_k^{*j})}}{\partial \vec{x}_0} \\ \frac{\partial F_{G,CS(\omega_k^{*j})}}{\partial \vec{x}_0} \end{bmatrix} = \begin{bmatrix} \frac{\partial C_q(\omega_k^{*j})}{\partial \vec{x}_0} \\ \frac{\partial S_q(\omega_k^{*j})}{\partial \vec{x}_0} \\ \frac{dCS_q(\omega_{k\pm 1}^{*j})}{\partial \vec{x}_0} \end{bmatrix}, \quad (73)$$

where $\frac{\partial \vec{F}_{G,j}}{\partial \vec{\xi}_j}$ is an invertible 3×3 matrix supplied via Eq. (65). The expressions on the right side of Eq. (73) involve expressions from Eq. (70) and are supplied in Appendix B. Then, it is possible to invert the matrix and write,

$$\begin{bmatrix} \frac{\partial \mathbf{f}_j}{\partial \vec{x}_0} \\ \frac{\partial A_j}{\partial \vec{x}_0} \\ \frac{\partial \theta_j}{\partial \vec{x}_0} \end{bmatrix} = \left(\frac{\partial \vec{F}_{G,j}}{\partial \vec{\xi}} \right)^{-1} \begin{bmatrix} \frac{\partial C_q(\omega_k^{*j})}{\partial \vec{x}_0} \\ \frac{\partial S_q(\omega_k^{*j})}{\partial \vec{x}_0} \\ \frac{dCS_q(\omega_{k\pm 1}^{*j})}{\partial \vec{x}_0} \end{bmatrix}, \quad (74)$$

deriving the sensitivities for the GMS-C approach.

4.2 Applications

Thus far, the Frequency-Domain Differential Corrector (FDDC) is derived within a general single-shooting formulation. The general aspects of the algorithm are further illustrated in the following examples focusing on the Distant Retrograde Orbits (DROs) and Elliptical Lunar Frozen Orbits (ELFOs).

4.2.1 Specifying a Quasi-Periodic Trajectory within the Distant Retrograde Orbit (DRO) Family

The Distant Retrograde Orbit (DRO) generally displays stable behavior across dynamical models and serves as a good example to test the single-shooting formulation. One such example is illustrated in Figs. 5(a) and 6(a), initiated with the state in Table 1. The initial state is propagated for 20 years in the CR3BP (Fig. 5(a)) and

the HFEM (Fig. 6(a)). Note that Eq. (2) is leveraged to rotate the BRF state into the JIF. An initial epoch of 2460576.5 in Julian Date (09/23/2024) is leveraged. Both CR3BP and HFEM display quasi-periodic behaviors, consistent with a previous observation by Bezrouk and Parker [40]. Note that the distance from the Moon to the x -axis crossing is approximately 22000 km.

An arbitrary goal is introduced to test the functionality of FDDC. Note that while the CR3BP dynamics allow $(n_i = 3)$ -dimensional QPOs for DRO-related structures, for simplicity, consider an in-plane motion where $z = z' = 0$. Then, two fundamental frequencies exist within the CR3BP framework: (1) ν_C , associated with the longitudinal period of the underlying DRO, and (2) ν_Q , associated with the in-plane quasi-periodic motion. The initial guess in Table 2 is generated by deliberately perturbing a state on a periodic DRO; the initial value $x' = 0.01$ does not satisfy the perpendicular crossing condition ($x' = 0$). The DFT on x -position components illustrate this behavior in Fig. 5(b), sampled with $N = 2^{16}$. In contrast to the DFT results for a Periodic Orbit (PO) (Fig. 3), the peaks now involve more than one fundamental frequency. Refining the first two peaks ($1 \leq j \leq 2$) with the L-NAFF algorithm, it is possible to identify the fundamental frequencies. The first peak f_1 coincides with ν_C , and the second peak f_2 coincides with ν_Q . The values for these fundamental frequencies are also confirmed from the monodromy matrix of the PO associated with the frequency of ν_C . The in-plane center eigenvalue is $\lambda_Q \approx 0.7362 \pm i0.6767$ associated with a rotation number of $\sigma_Q = \arctan 2(|\text{Im}(\lambda_Q)|, \text{Re}(\lambda_Q)) \approx 0.7433$ (rad). Noting that the rotation number is connected to the frequency as $\sigma_Q = 2\pi\nu_Q/\nu_C$, the second fundamental frequency from the monodromy matrix is retrieved as $\nu_Q \approx 1.0249 \approx f_2$ (Fig. 5(b)). Of course, depending on the magnitude along the quasi-periodic oscillation, ν_Q may coincide with the second dominant peak. Such a case is often observed within the HFEM. Figure 6 illustrates the counterpart behavior within the HFEM. The initial BRF state from Table 1 is rotated into the JIF on 09/23/2024, propagated within the HFEM and rotated back to BRF for consistent visualization. With the external perturbations, the DRO now tracks a more dispersed behavior as evidenced in Fig. 6(a). The corresponding Fourier domain response is recorded in Fig. 6(b) with $q = x$ as consistently defined with the CR3BP investigation from Figure 5(b). The most dominant peak, f_1 , still coincides with ν_C . Note that the exact value for ν_C may be subject to change from the CR3BP value as it is not explicitly controlled in the rotation process (Eq. (2)). In contrast to the CR3BP case, the HFEM trajectory does not supply $f_2 \approx \nu_Q$. Rather, f_2 is associated with the convoluted frequency between ν_C and ν_Q . Refining frequencies associated with subsequent peaks, ν_Q now coincides with f_5 , the fifth dominant frequency. While it is more trivial to locate and target the most dominant frequency, ν_C in this case, it is more nuanced to detect the secondary frequency, i.e., ν_Q . The situation is more challenging within the HFEM due to the presence of the external frequencies that generate multiple peaks that do not originally exist within the CR3BP dynamics. The frequency structures in Figs. 5(b) and 6(b) are summarized in Tables 3 and 4, respectively.

Assume that the fundamental frequencies, ν_C and ν_Q , are desired to be adjusted. The following (arbitrary) frequency structure is enforced,

$$\text{For } \nu_C : \begin{bmatrix} f_j - 8.66331279836 \\ \theta_j - \pi \end{bmatrix} = 0, \quad \text{For } \nu_Q : \begin{bmatrix} A_j - 0.001 \\ \theta_j - \pi/8 \end{bmatrix} = 0. \quad (75)$$

Within the CR3BP, examining the spectrum from Fig. 5(b), f_j with $j = 1, 2$ are *identified* as ν_C and ν_Q , respectively. During the corrections process within FDDC, however, the ordering of the secondary peaks may change. Alternatively, thus, the index j is recovered corresponding to the frequency bin that displays the j -th peak, i.e., ω_k^{*j} , closest to $\nu_Q \approx 1.02597$ (HFEM). As the value for ν_Q , of course, changes during the corrections, these two strategies, i.e., (1) fixing the index j and (2) investigating the frequency ν_Q supplied *a priori*, are complementary to each other. Also note that the convoluted frequency $\nu_C + \nu_Q$ may be dominant compared to the fundamental frequency ν_Q itself as apparent within the HFEM (Fig. 6(b)). It is possible to employ FDDC on convoluted frequencies, an approach not explored in the current investigation.

The FDDC process is employed for both the CR3BP and HFEM to satisfy the target frequency structure from Eq. (75). The resulting geometries are illustrated in Fig. 7. The red curves within the plots correspond to the invariant curve (CR3BP) and invariant surface (HFEM), respectively, recorded every passage of $2\pi/\nu_C$ in the nd time, eliminating the dependency on one of the fundamental frequencies. As the phase angle for ν_C is targeted as $\theta_j = \pi$, the invariant curve (surface) appears to the left of the Moon (Eq. (12)). The corresponding frequency structures are included in Tables 5 and 6. The targeted frequency components are marked with

✓, converged below the set tolerance, $1 \cdot 10^{-10}$ (nd). The initial state for the CR3BP and HFEM along the targeted trajectories are included in Tables 7 and 8, respectively. Compared to the original geometries from Figs. 5(a) and 6(a), the targeted frequency structures are associated with larger A_j for ν_Q and appear to be more dispersed within the BRF. The current example on the DRO demonstrates the capabilities of FDDC to specify trajectories on a QPO across models of varying fidelity. Specifically, the HFEM trajectory likely tracks higher-dimensional QPO with $n \geq 7$. The proposed algorithm, i.e., FDDC, is capable of targeting n_i (internal) frequencies, avoiding the complexity of explicitly considering n frequencies simultaneously. Note that the out-of-plane quasi-periodic motion also exists that is not explicitly considered in this example. Without an explicit control of such components, the corrections process in FDDC may introduce components into the third direction. Note that while \vec{X}_0 , the free variable vector, is six-dimensional, \vec{F}_f (Eq. (66)) is a four-dimensional vector. A minimum-norm approach is leveraged to supply the search direction for the differential corrector.

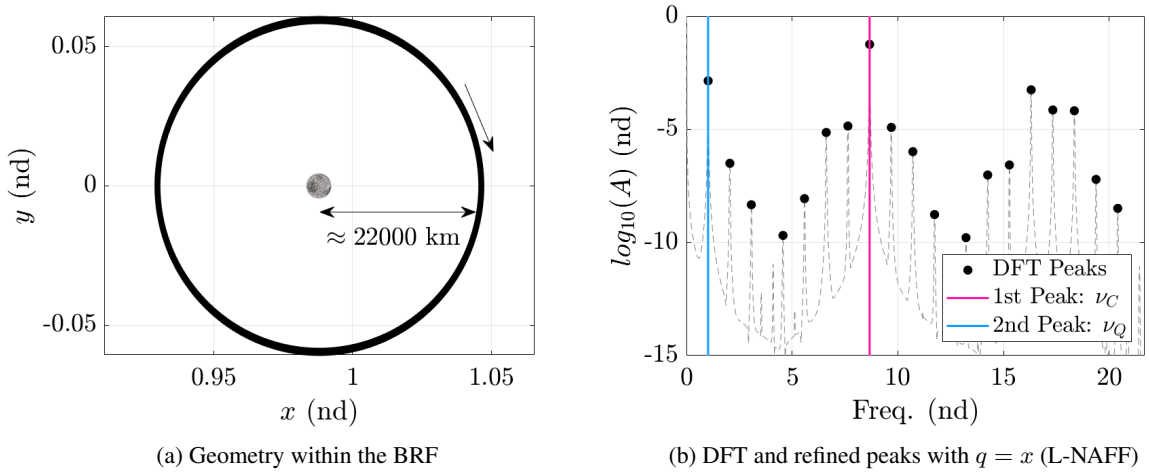


Fig. 5: CR3BP quasi-DRO initiated with the state in Table 2

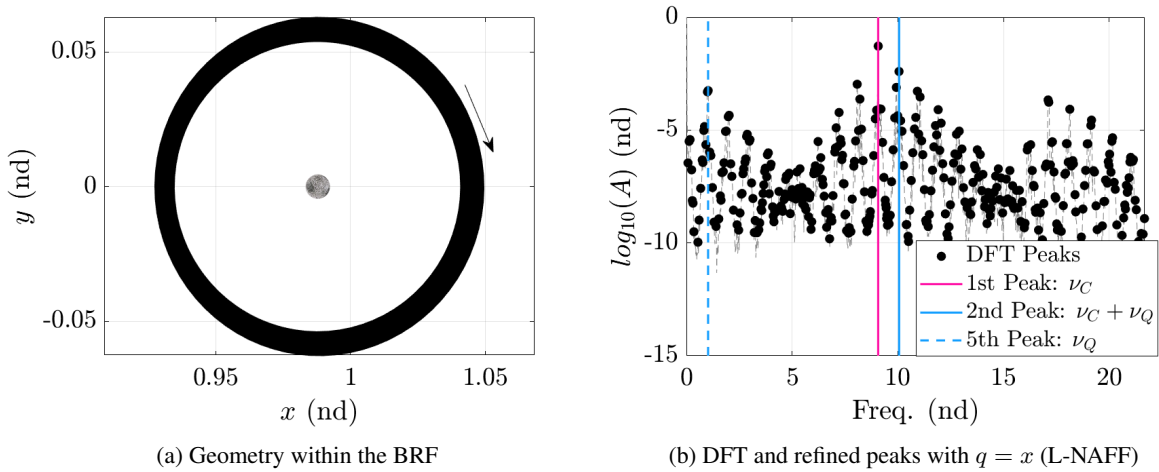


Fig. 6: HFEM quasi-DRO initiated with the state in Table 2

Table 2: Initial state \vec{X}_0 for the quasi-DRO (Figs. 5 and 6)

Component	Value
x	0.929817046666844
y	0
z	0
x'	0.01
y'	0.522717065584611
z'	0

Table 3: Initial frequency structure for the CR3BP quasi-DRO propagated with Table 2

	$\nu_C (j = 1)$	$\nu_Q (j = 2)$
f_j	8.663312798420872	1.024930860632975
A_j	0.058190266942043	0.001425616315091
θ_j	-3.098796017720698	1.571460016637346

Table 4: Initial frequency structure for the HFEM quasi-DRO propagated with Table 2

	$\nu_C (j = 1)$	$\nu_Q (j = 5)$
f	9.067270092334322	1.025971597715591
A	0.056230858215909	0.000563726693198
θ	3.062426060730863	2.257364738089462

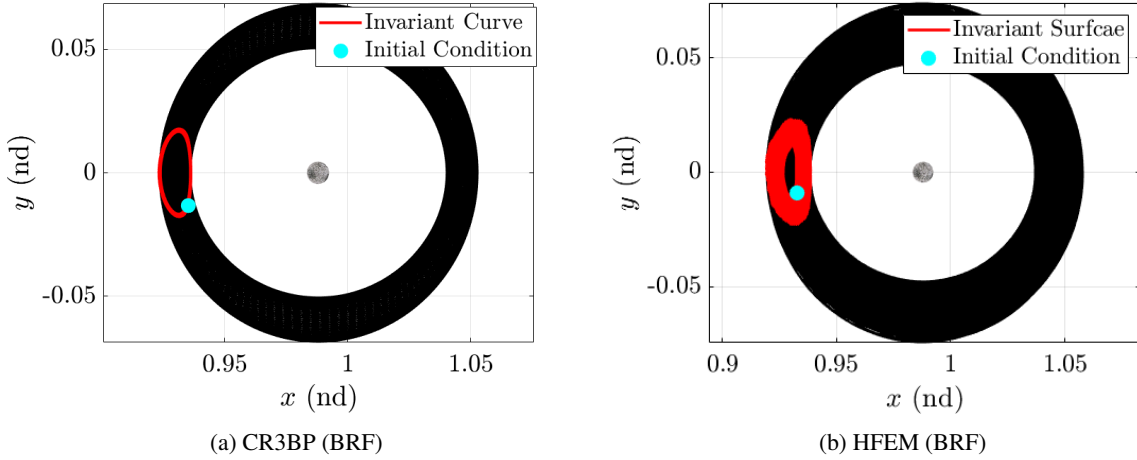


Fig. 7: Targeted quasi-DRO

Table 5: Targeted frequency structure for the CR3BP quasi-DRO propagated with Table 7 (✓: targeted)

	$\nu_C (j = 1)$	$\nu_Q (j = 2)$
f_j	8.663312798369873 ✓	1.025840351634718
A_j	0.057630566792085	0.009999999891364 ✓
θ_j	3.141592655033092 ✓	0.785398163502869 ✓

4.3 Elliptical Lunar Frozen Orbit (ELFO) Constellation Design

Elliptical Lunar Frozen Orbits (ELFOs) offer an attractive option to support various missions in the lunar vicinity. These orbital structures supply near-stability over a long horizon time and the ability to provide extended line-of-sight to the Lunar South Pole (LSP), a key region for expanding cislunar space activities in

Table 6: Targeted frequency structure for the HFEM quasi-DRO propagated with Table 8 (✓: targeted)

	$\nu_C (j = 1)$	$\nu_Q (j = 5)$
f_j	8.663312798372578 ✓	1.026122000070913
A_j	0.057532681072891	0.009999999998136 ✓
θ_j	3.141592653498086 ✓	0.785398163697401 ✓

Table 7: Targeted initial state $\vec{\mathbb{X}}_0$ for the quasi-DRO, CR3BP (Fig. 5(a))

Component	Value
x	0.935182071235081
y	-0.013296687505060
z	0
x'	-0.071999754120518
y'	0.542602051432254
z'	0

Table 8: Targeted initial state $\vec{\mathbb{X}}_0$ for the quasi-DRO, HFEM (Fig. 6(a))

Component	Value
x	0.932714478796438
y	-0.009071158291536
z	-0.000720383507459
x'	-0.018764477779327
y'	0.543649830698251
z'	0.000579106771136

the near future [41]. Leveraging these benefits, multiple space entities envision the inclusion of one or more satellites in ELFOs²³ as a part of a data relay system. The ELFOs satisfy the “frozen” condition, admitting nearly constant *mean* eccentricity, inclination, and argument of perilune [35]. While a variety of orbits supply such a condition, the ELFOs are characterized by relatively high altitude, inclination and eccentricity values, where the point-mass Earth gravity significantly contributes to the stable evolution of the orbit geometry [30].

The ELFOs exist in the vicinity of the equilibria derived from the simplified, Doubly-Averaged Dynamical Model (DADM) [35, 30, 31, 42]. From the equations of motion as represented in the doubly-averaged orbital elements from Eqs. (4)-(9), observe that the dynamics for $\bar{e}, \bar{i}, \bar{\omega}$ are separable. Then, the following equilibrium conditions specify the ELFOs,

$$\bar{\omega}_{eq} = \pi/2, 3\pi/2 \quad (76)$$

$$\bar{e}_{eq} = \sqrt{1 - 5/3 \cos^2 \bar{i}_{eq}}. \quad (77)$$

The equilibria are elliptic, i.e., they admit nearby periodic orbits in terms of $\bar{e}, \bar{i}, \bar{\omega}$. This period is denoted as the *long-period* and constitutes one of the fundamental frequencies, ν_L , for the ELFOs. While specific values differ by the combinations of $\bar{e} - \bar{i} - \bar{\omega}$, it is generally associated with periods on the order of one year. Recall that the DADM is integrable in the Liouville-Arnold sense [1, 35] where every solution generally appears as an $(n_i = 3)$ -dimensional quasi-periodic orbit. Thus, two more fundamental frequencies exist that are associated with the averaged angles. The *short-period* corresponds to one complete revolution for \bar{M} , that depends on \bar{a} , and is on the order of one day. The *medium-period* is associated with the passage of 2π (radians) for the modified right ascension defined as $\bar{\Omega}_M = t - \bar{\Omega}$ as measured clockwise within the BR

²<https://www.intuitivemachines.com/post/nasa-selects-intuitive-machines-to-deliver-4-lunar-payloads-in-2024>, Accessed: 09-05-2024

³<https://spacenews.com/china-could-develop-dual-relay-satellite-system-for-earth-moon-communications-to-reduce-geopolitical-risks>, Accessed: 09-05-2024

such that the rate of $\bar{\Omega}_M$ is positive. Noting that $d\bar{\Omega}/dt < 0$ for $\bar{\omega} = \pi/2$ and $\bar{i} \leq \pi/2$ (Eq. (8)), the period for $\bar{\Omega}_M$ is slightly larger than 2π , on the order of one month. The fundamental frequencies for the ELFOs and structures in the near vicinity are, thus, comprised of ν_S, ν_M, ν_L , associated with the short-, medium-, and long-period of the system. The ELFOs pertain to the specific case where the Eqs. (76) and (77) are satisfied and the long-period frequency ν_L is defined only in a limiting sense.

While the ELFOs are initially derived in the simplified DADM, the trajectories must be *refined* within the Higher-Fidelity Ephemeris Model (HFEM) such that they are suitable for actual flight. One challenge exists in defining a suitable transformation between the doubly-averaged orbital elements and the osculating elements (Fig. 1). While both semi-analytical [35] and fully-numerical strategies [43, 44] appear in the literature to supply the transformation, a systematic corrections process remains elusive to refine ELFOs within a higher-fidelity model. For designing and operating a satellite *constellation* within ELFOs, the capabilities to refine ELFOs within a higher-fidelity model are increasingly important. The constellation introduces phase constraints between the satellites, necessitating precise initial states to maintain these constraints throughout the mission timeline.

The proposed FDDC approach is well-suited for a satellite constellation as the phasing information is explicitly enforced during the corrections process. The following numerical example demonstrates its capabilities within the context of the ELFO constellation. Consider an arbitrary constellation comprised of three satellites. The initial states are derived initially from the DADM, included in Table 9, designed to provide coverage of the lunar south pole ($\bar{\omega} = 90^\circ$) for approximately 10 years. The combination of $\bar{e}, \bar{i}, \bar{\omega}$ satisfy the conditions from Eqs. (76) and (77). Phasing requirements are set such that the satellites are separated by 120° in both $\bar{\Omega}$ and \bar{M} , ensuring consistent coverage. While this requirement suggests initial guesses for $\bar{\alpha}$ (a symbol defined in Section 2) offset by 120° in $\bar{\Omega}$ and \bar{M} , the transformed states $\bar{\mathbf{X}}_0$ (represented in the JIF) in the HFEM often fail to meet the desired phasing upon test propagation, requiring adjustments. For the examples presented, the initial epoch is fixed on 09/23/2024. The resulting trajectories are visualized in Fig. 8(a) leveraging the BRF as the reference frame. The plots depict the first ≈ 1.3 days of propagation. Over longer periods, however, phase drift in M and Ω is observed, as apparent in Fig. 8(b). The vertical axis illustrates ΔM and $\Delta \Omega$, that is, the relative phasing between the satellites within the constellation over time. This phase drift negatively impacts the constellation's ability to maintain consistent coverage and line-of-sight.

The first satellite, i.e., Sat 1, is further examined to supply insights regarding the geometric interpretations for the drift and the fundamental frequencies, i.e., ν_S, ν_M, ν_L . The geometry is depicted within BRF in Fig. 9(a) for the first ≈ 10 years. Note that the orbital plane rotates clockwise within the BRF. As the short-period frequency ν_S is closely related to \bar{M} , and from the shape of the orbit, $q = z$ is examined. The resulting spectrum is plotted in Fig. 9(b), where the most dominant peak tracks $\nu_S \approx 26$ (nd), refined with the GMS-C method. However, as the medium-period frequency, ν_M , is associated with $\bar{\Omega}_M$, it is rather challenging to extract the information directly from z . Thus, $q = x$ is examined and plotted in Fig. 9(c), where the second peak (\mathbf{f}_j) tracks ν_M , also refined with the GMS-C algorithm. The initial condition derived within the DADM satisfies the equilibrium condition from Eqs. (76)-(77), eliminating the peaks associated with the long-period frequency ν_L within the DADM (tracking a 2-dimensional QPO). However, due to the limited accuracy of the transformation process described in Fig. 1, trajectories within the HFEM typically excite the oscillatory mode into the ν_L -direction. This long-period (low) frequency is associated with a low amplitude, requiring extra caution in proper detection. One requirement is a long propagation time such that $\Delta\omega \ll 1$ to resolve the low frequency $\nu_L < 0.1$ (on the order of years). Note that this lower-frequency-domain is challenging to visually detect within the spectra included in Fig. 9. One possible complementary strategy is to leverage a stroboscopic map with a period of $2\pi/\nu_S$, eliminating the influence of the short-period frequency ν_S . The states at the stroboscopic map are illustrated in Fig. 10(a), marking the first $N = 2^{14}$ returns to the map. The DFT results are included in Fig. 10(b) with $q = x$. While the HFEM alone demonstrates multiple peaks due to the impact from the n_e external frequencies, the auxiliary analysis from the CR3BP initiated with the same initial state (from Table 10, transformed with Fig. 1) supplies well-defined peaks and a reference number for $\nu_L \approx 0.057$ (nd).

Table 9: Set of doubly-averaged mean orbital elements for the three-satellite constellation

$\bar{\alpha}$	\bar{a}	\bar{e}	\bar{i}	$\bar{\Omega}$	$\bar{\omega}$	\bar{M}
Value	10,000 (km)	0.4082 (nd)	45°	0°, 120°, 240°	90°	180°, 300°, 60°

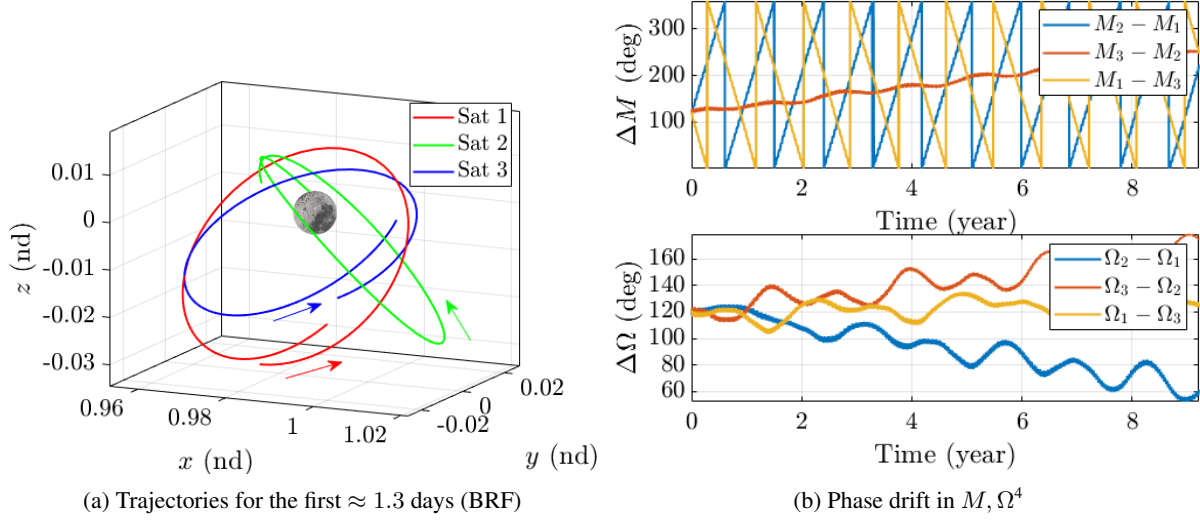


Fig. 8: Initial guess for the three-satellite constellation with undesired phase drift

⁴Note that the desired phase drift values for M, Ω are 120° on average. The subscripts 1, 2, 3 denote Sat 1, 2, 3; for example, $M_2 - M_1$ corresponds to the phase difference in M between Sat 2 with respect to Sat 1. The same description applies to Fig. 11(b) as well.

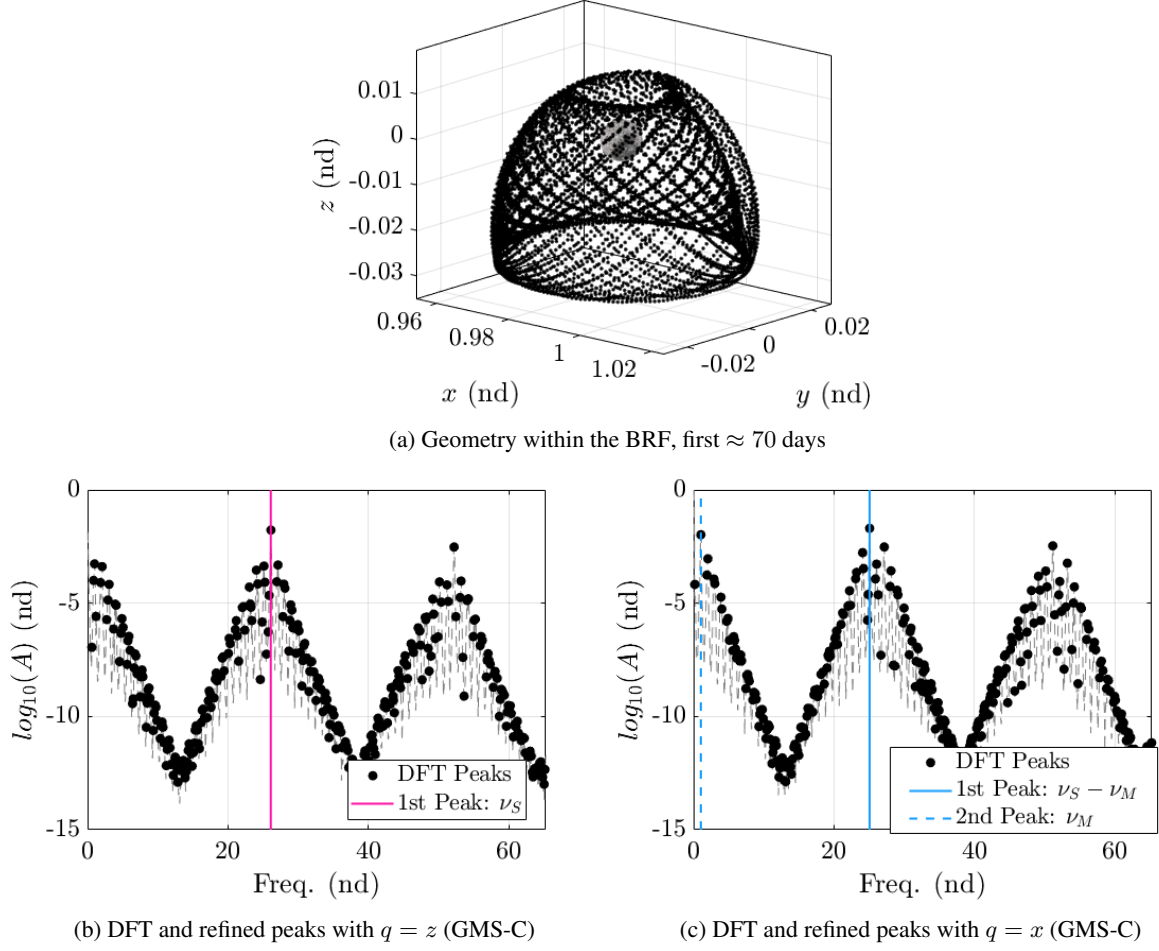


Fig. 9: HFEM ELFO (Sat 1) initiated with the state in Table 10

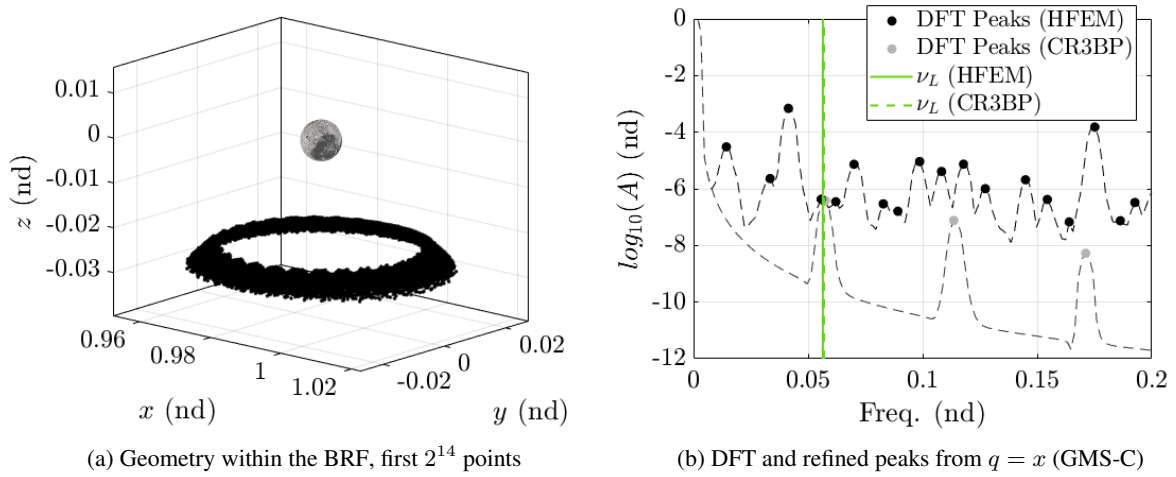


Fig. 10: Stroboscopic map along the HFEM ELFO (Sat 1) initiated with the state in Table 10

With this geometric interpretation of the fundamental frequencies, the initial configuration for the ELFO constellation from Fig. 8 is revisited. The initial state and frequency structure for each of the satellites are included in Table 10. Note that the initial state \vec{X}_0 is represented in the inertial frame (JIF), but the signals for the DFT are constructed within the rotating frame (BRF), e.g., x . Thus, the partial in Eq. (70) is evaluated with,

$$q = x = [1, 0, 0] \vec{\rho} = [1, 0, 0] \frac{l_*}{l} \mathbf{C}^T \vec{R} + \vec{\rho}_M, \quad (78)$$

from Eq. (2). Then,

$$\frac{dq(t_i)}{d\vec{X}_0} = \frac{dq(t_i)}{d\vec{X}^{t_i}(\vec{X}_0; \mathbf{t}_0)} \frac{d\vec{X}^{t_i}(\vec{X}_0; \mathbf{t}_0)}{d\vec{X}_0} = [1, 0, 0] \frac{l_*}{l} \mathbf{C}^T \phi^{t_i}(\vec{X}_0; \mathbf{t}_0)_{3 \times 6}. \quad (79)$$

The subscript 3×6 denotes that a sub-matrix of the STM is leveraged that is connected to the position at sample time t_i . The direction cosine matrix \mathbf{C} is also evaluated at time t_i . A similar process is extended to $q = z$ as well. The frequency structures included in Table 10 consist of five different quantities: frequency and phase angles for short- and medium-period frequencies, and the amplitude associated with the long-period frequency. Note that these fundamental frequencies and the associated phase angles are retrieved from the frequency refinement analysis in Fig. 9. Arrows indicate whether components overshoot (\uparrow) or undershoot (\downarrow) their desired values with respect to Sat 1. For example, Sat 1 employs an initial guess $\nu_S = 26.0840$ (nd), while Sat 2 and Sat 3 exhibit slightly higher values (overshot, \uparrow). The initial design intends for Sat 2 and Sat 3 to lead and lag Sat 1 by 120° , respectively. However, these small deviations in ν_S prevent these satellites from maintaining the desired phase offset, as evident in Fig. 8(b). Similar behavior is observed for ν_M , where the relative configuration for Ω deteriorates over time. Note that $\theta_S \approx \bar{M}$ and $\theta_M \approx \bar{\Omega}_M$, although not exactly. Furthermore, the initial phase offsets for ν_S and ν_M deviate slightly from the desired 120° due to limitations in the transformation accuracy described in Fig. 1. For instance, Sat 2 initially leads Sat 1 in θ_S by only 106° , falling short by 14° for the intended offset (undershot \downarrow). For all three satellites, the trajectories are associated with small amplitudes for the long-period frequency ν_L examined with $q = x$, i.e., $A_L < 1 \cdot 10^{-6}$ (nd). The phase angles for this oscillatory mode are not illustrated in Table 10.

Utilizing the frequency-domain targeter, the state vectors \vec{X}_0 are refined to eliminate the phase drift. The following constraint vector is arbitrarily enforced,

$$\text{For } \nu_S : \begin{bmatrix} \mathbf{f}_j - 26.1685 \\ \Delta\theta_j - (\pm 120^\circ) \end{bmatrix}, \quad \text{For } \nu_M : \begin{bmatrix} \mathbf{f}_j - 1.0341 \\ \Delta\theta_j - (\pm 120^\circ) \end{bmatrix}, \quad \text{For } \nu_L : [A_j - 1 \cdot 10^{-6}] < 0. \quad (80)$$

For Sat 1, the phase angles $\theta_{S,M}$ are not targeted as it is assumed to serve as an arbitrary reference satellite within the constellation. After Sat 1 is targeted with Eq. (80), the remaining satellites are adjusted relative to Sat 1 with phase offsets of $\pm 120^\circ$. The long-period frequency component, ν_L , is not explicitly targeted. Rather, it is assumed that the quasi-periodic oscillation amplitude in x associated with $\nu_L \approx 0.057$ (nd) is desired to be capped at $1 \cdot 10^{-6}$ (nd). Solving Eq. (80) using a minimum-norm approach ensures that A_j (the oscillation magnitude in x) does not significantly deviate from its original value for ν_L ; while A_j is monitored for ν_L , it is not explicitly constrained in this example. The resulting state vectors \vec{X}_0 are provided in Table 10. The frequency structures are now fully targeted successfully, as indicated by green check marks (\checkmark). The targeted frequencies ν_S and ν_M match within a tolerance of $1 \cdot 10^{-7}$ (nd), and the initial phase angles are set to be 120° apart with a tolerance of $1 \cdot 10^{-7}$ radians. This information is confirmed by examining the evolution of the relative M, Ω angles over ≈ 10 years as plotted in Fig. 11(b). While the oscillations exist due to the nature of the osculating elements (α), it is obvious that the relative phasing across the constellation remains stable, ensuring consistent performance.

The proposed FDDC strategy provides multiple benefits in constellation design and operation leveraging ELFOs. While manually adjusting the initial guesses provided by the DADM achieves a desired constellation, the current approach offers a scalable, automatable scheme to reference constellation design. The frequency-domain constraints are seamlessly integrated with other mission requirements, enabling a systematic search

⁵The angles $\Delta\theta_S, \Delta\theta_M$ are defined with respect to Sat 1.

Table 10: ELFO constellation constructed on 09/23/2024 (✓: targeted, ⬆: overshoot, ⬇: undershoot) ⁵

Sat No.	Initial guess			Targeted and converged		
	Sat 1	Sat 2	Sat 3	Sat 1	Sat 2	Sat 3
ν_S (nd)	26.0840 (N/A)	26.1687 (⬆0.09)	26.1685 (⬆0.09)	26.1685 (N/A)	26.1685 (✓)	26.1685 (✓)
$\Delta\theta_S$ (deg)	0° (N/A)	106° (⬇14°)	242° (⬆2°)	0° (N/A)	120° (✓)	240° (✓)
ν_M (nd)	1.0341 (N/A)	1.0367 (⬆0.026)	1.0327 (⬇0.014)	1.0341 (N/A)	1.0341 (✓)	1.0341 (✓)
$\Delta\theta_M$ (deg)	0° (N/A)	133° (⬆13°)	235° (⬇5°)	0° (N/A)	120° (✓)	240° (✓)
A_L (nd)	$< 1 \cdot 10^{-6}$	$< 1 \cdot 10^{-6}$	$< 1 \cdot 10^{-6}$	$< 1 \cdot 10^{-6}$	$< 1 \cdot 10^{-6}$	$< 1 \cdot 10^{-6}$
X (nd)	2.3681 ·10 ⁻²	-2.4116 ·10 ⁻²	-1.8681 ·10 ⁻²	2.3046 ·10 ⁻²	-2.4121 ·10 ⁻²	-1.8170 ·10 ⁻²
Y (nd)	3.9275 ·10 ⁻³	4.3168 ·10 ⁻³	1.5963 ·10 ⁻²	4.5786 ·10 ⁻³	4.4484 ·10 ⁻³	1.6671 ·10 ⁻²
Z (nd)	-2.7631 ·10 ⁻²	-3.4412 ·10 ⁻³	2.8722 ·10 ⁻³	-2.7283 ·10 ⁻²	-2.4864 ·10 ⁻³	2.5967 ·10 ⁻³
X' (nd)	1.6878 ·10 ⁻¹	1.4913 ·10 ⁻¹	-4.5236 ·10 ⁻¹	1.7087 ·10 ⁻¹	1.5159 ·10 ⁻¹	-4.4563 ·10 ⁻¹
Y' (nd)	3.6168 ·10 ⁻¹	-6.7205 ·10 ⁻¹	2.2267 ·10 ⁻²	3.7412 ·10 ⁻¹	-6.7573 ·10 ⁻¹	2.5913 ·10 ⁻²
Z' (nd)	1.9606 ·10 ⁻¹	2.0540 ·10 ⁻¹	-5.5763 ·10 ⁻¹	1.9643 ·10 ⁻¹	1.9973 ·10 ⁻¹	-5.6094 ·10 ⁻¹

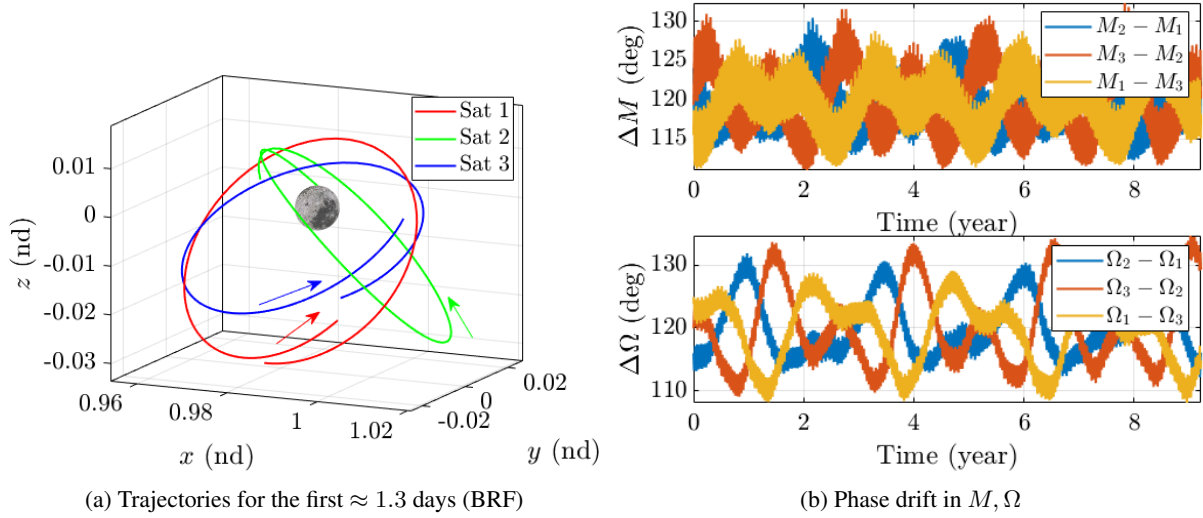


Fig. 11: Targeted and converged three-satellite ELFO constellation with controlled phase drift

for optimal constellations. This strategy also delivers precise control over some frequency coordinates, a task that is difficult to accomplish through manual orbital element adjustments. For example, although the semi-major axis (\bar{a} or a) primarily influences ν_S , all orbital elements collectively affect the frequency structure. Similarly, achieving a phase separation of 120° among three satellites is not naturally achievable solely via orbital element adjustments. Instead, this FDDC technique directly and accurately targets such configurations. Although this application focuses on reference constellation design, the Jacobian matrix $\partial \vec{F} / \partial \vec{X}_0$ and its inverse provide valuable operational insights. For example, the impact of stochastic errors in

the spacecraft state on downstream phasing information is linearly predicted using the matrix $\partial \vec{F}/\partial \vec{X}_0$. This predictive capability enhances operational robustness.

5 Frequency-Domain Differential Corrector (FDDC): Multiple-Shooting Formulation

Depending on the dynamical regime, the signal q may not be generated from a single, long propagation from an initial state, \vec{X}_0 . In many environments associated with instability, such a long propagation likely excites nearby hyperbolic manifolds, destroying the quasi-periodic behavior. In such a case, a multiple-shooting formulation typically aids in construction of the long-term trajectories [45, 46] and retrieval of QPOs. In a similar context, FDDC is extendable to multiple-shooting formulation. Consider the following sequence of state vectors,

$$\vec{X} = [\vec{X}_0, \vec{X}_1, \vec{X}_2, \dots, \vec{X}_{n_p-1}], \quad (81)$$

where n_p is the number of patchpoints along the trajectory. The initial epochs (for a non-autonomous case, e.g., the HFEM) corresponding to the patchpoints are predetermined (by assumption) as,

$$[\mathbf{t}_0, \mathbf{t}_1, \mathbf{t}_2, \dots, \mathbf{t}_{n_p}], \quad (82)$$

where the propagation time is also assumed to be fixed as,

$$\Delta \mathbf{t}_{i_s} = \mathbf{t}_{i_s+1} - \mathbf{t}_{i_s} \quad (0 \leq i_s \leq n_p - 1). \quad (83)$$

A typical multiple shooter to ensure the continuity between the patchpoints then enforces,

$$\vec{F}_p = \begin{bmatrix} \vec{X}^{\Delta \mathbf{t}_0}(\vec{X}_0; \mathbf{t}_0) - \vec{X}_1 \\ \vec{X}^{\Delta \mathbf{t}_1}(\vec{X}_1; \mathbf{t}_1) - \vec{X}_2 \\ \dots \\ \vec{X}^{\Delta \mathbf{t}_{n_p-2}}(\vec{X}_{n_p-2}; \mathbf{t}_{n_p-2}) - \vec{X}_{n_p-1} \end{bmatrix} = \vec{0}, \quad (84)$$

where the expression \vec{X} is defined from Eq. (68). For example, $\vec{X}^{\Delta \mathbf{t}_0}(\vec{X}_0; \mathbf{t}_0)$ denotes the downstream state propagated from the initial state and epoch of \vec{X}_0 and \mathbf{t}_0 , respectively, for the duration of $\Delta \mathbf{t}_0$. Note that Eq. (84) is a vector of length $6(n_p - 1)$ while the length of \vec{X} is $6n_p$. Thus, targeting solely for the continuity between the patchpoints lacks proper boundary constraints, resulting in an underconstrained problem [47]. The Jacobian matrix for \vec{F}_p with respect to \vec{X} is constructed as,

$$\frac{\partial \vec{F}_p}{\partial \vec{X}} = \begin{bmatrix} \phi^{\Delta \mathbf{t}_0}(\vec{X}_0; \mathbf{t}_0) & -\mathbf{I}_{6 \times 6} & \mathbf{0}_{6 \times 6} & \mathbf{0}_{6 \times 6} & \dots & \mathbf{0}_{6 \times 6} & \mathbf{0}_{6 \times 6} \\ \mathbf{0}_{6 \times 6} & \phi^{\Delta \mathbf{t}_1}(\vec{X}_1; \mathbf{t}_1) & -\mathbf{I}_{6 \times 6} & \mathbf{0}_{6 \times 6} & \dots & \mathbf{0}_{6 \times 6} & \mathbf{0}_{6 \times 6} \\ \vdots & \vdots & \vdots & \vdots & \ddots & \vdots & \vdots \\ \mathbf{0}_{6 \times 6} & \mathbf{0}_{6 \times 6} & \mathbf{0}_{6 \times 6} & \mathbf{0}_{6 \times 6} & \dots & \phi^{\Delta \mathbf{t}_{n_p-2}}(\vec{X}_{n_p-2}; \mathbf{t}_{n_p-2}) & -\mathbf{I}_{6 \times 6} \end{bmatrix}. \quad (85)$$

The extension of FDDC into a multiple-shooting formulation builds on this typical continuity corrector defined with the free variable vector (Eq. (81)), constraint (Eq. (84)), and the Jacobian matrix (Eq. (85)).

5.1 Sensitivities of the State Vectors on the Frequency Components

In addition to the continuity constraint \vec{F}_p (Eq. (84)), the frequency-domain constraint \vec{F}_f (Eq. (66)) is included to formulate FDDC within the multiple-shooting environment. To this end, the sensitivity vectors defined from the single-shooting formulation (Sect. 4.1) are extended to their multiple-shooting formulation counterparts. Specifically, Eq. (67) is now generalized to the multiple-shooting formulation as,

$$\frac{\partial \mathbf{f}_j}{\partial \vec{X}}, \frac{\partial A_j}{\partial \vec{X}}, \frac{\partial \theta_j}{\partial \vec{X}}, \quad (86)$$

where a single vector \vec{X}_0 from Eq. (67) is extended to the multiple patchpoint state vectors in Eq. (81).

5.1.1 Sensitivities within the Laskar-Numerical Analysis of Fundamental Frequency (L-NAFF) Method

A similar process from the single-shooting formulation is repeated. Differentiating the constraint vector (Eq. (48)) and inverting a matrix yields,

$$\begin{bmatrix} \frac{\partial \mathbf{f}_j}{\partial \vec{\mathbf{x}}} \\ \frac{\partial A_j}{\partial \vec{\mathbf{x}}} \\ \frac{\partial \theta_j}{\partial \vec{\mathbf{x}}} \end{bmatrix} = - \left(\frac{\partial \vec{F}_{L,j}}{\partial \vec{\xi}_j} \right)^{-1} \begin{bmatrix} \frac{\partial F_{L,f}}{\partial \vec{\mathbf{x}}} \\ \frac{\partial F_{L,c}}{\partial \vec{\mathbf{x}}} \\ \frac{\partial F_{L,s}}{\partial \vec{\mathbf{x}}} \end{bmatrix}. \quad (87)$$

where the left side corresponds to a $(3 \times 6n_p)$ matrix. The expressions for the right side are supplied in Appendix C.

5.1.2 Sensitivities within the Gómez-Mondelo-Simó-Collocation (GMS-C) Method

A similar process is now initiated with the GMS-C method. Differentiating Eq. (64) yields,

$$\begin{bmatrix} \frac{\partial \mathbf{f}_j}{\partial \vec{\mathbf{x}}} \\ \frac{\partial A_j}{\partial \vec{\mathbf{x}}} \\ \frac{\partial \theta_j}{\partial \vec{\mathbf{x}}} \end{bmatrix} = \left(\frac{\partial \vec{F}_{G,j}}{\partial \vec{\xi}} \right)^{-1} \begin{bmatrix} \frac{\partial C_q(\omega_k^{*j})}{\partial \vec{\mathbf{x}}} \\ \frac{\partial S_q(\omega_k^{*j})}{\partial \vec{\mathbf{x}}} \\ \frac{dC S_q(\omega_{k \pm 1}^{*j})}{\partial \vec{\mathbf{x}}} \end{bmatrix}, \quad (88)$$

deriving the sensitivities for the GMS-C approach. Expressions for the right side are supplied in Appendix C.

5.2 Application: Controlling Quasi-Periodic Motion in Near Rectilinear Halo Orbit (NRHO)

The capabilities of the multiple shooter formulation within the frequency-domain are demonstrated on a sample scenario that involves the 9 : 2 synodic resonant Near Rectilinear Halo Orbit (NRHO). This NRHO is envisioned to serve as a baseline orbit for NASA's Gateway mission. Note that a numerical approach already exists in literature [48] to supply a long-term baseline solution. However, due to the underconstrained nature of the problem from Eq. (84), the solution generated within the HFEM may display seemingly “random” behavior depending on the numerical process employed. Brown et al. [21] also investigate the quasi-periodic trajectories that exist in the vicinity of the 9 : 2 NRHO, contributing to the expansion of the available solution space. The proposed approach, i.e., FDDC, serves as a complementary approach to pinpoint the solution via explicitly controlling the quasi-periodic motion.

Several dynamical features regarding the 9 : 2 NRHO within the CR3BP are first reviewed, followed by initial observations in the frequency-domain. Within the CR3BP, the monodromy matrix for the 9 : 2 halo admits the following 6 eigenvalues: $\approx [1, 1, -2.1783, -0.4591, 0.6845 \pm i0.7290]$. Note that the unity pair corresponds to the along-orbit and along-family directions. The real reciprocal pair corresponds to the hyperbolic modes, i.e., the stable and unstable modes of the orbit. The complex conjugate pair denotes the oscillatory (center) mode, giving rise to the quasi-periodic motion nearby. Being a 9 : 2 *synodic* NRHO, the fundamental frequency corresponding to the underlying period is $\nu_C = 4.1633$ (nd). The second fundamental frequency is $\nu_Q \approx 0.5415$ (nd), supplied from the center eigenvalues. Due to the existence of the hyperbolic modes, the maximal dimension of the QPO within the CR3BP for this orbit is $n_i = 2$. Utilizing the GMOS [15, 16] algorithm, a sample 2D-QPO within the CR3BP is targeted as illustrated in Fig. 12(a). The quasi-periodic nature is apparent from the width of the trajectory within the BRF. The corresponding frequency-domain analysis is included in Fig. 12(b) for $q = x$. For this specific case, the first dominant peak corresponds to the ν_C , and the third dominant peak tracks ν_Q . The shape of the NRHO is more visually “elliptical” as opposed to the DRO (Fig. 5) within the BRF. Thus, more DFT samples N aid in preventing aliasing in general as the amplitudes decay at a slower rate for the NRHO. Thus, $N = 2^{20}$ is set for the NRHO. Leveraging the QPO from the CR3BP as an initial guess, a counterpart (continuous) trajectory within the HFEM is supplied as visualized in Fig. 13(a). A multiple-shooting algorithm is employed, similar to the formulation from Eqs. (81) and (84) [48]. Over 20 years of total propagation, three patchpoints are placed

per revolution as illustrated in Fig. 13(a). The geometry is more dispersed compared to the CR3BP QPO within BRF. The spectrum also displays complex behavior within the HFEM in Fig. 13(b). The fundamental frequencies ν_C and ν_Q coincide with the 1st and 8th peak, respectively, refined with the L-NAFF algorithm. The frequency structure for this HFEM quasi-periodic trajectory is illustrated in Table 11 with the frequency, amplitude, and phase angle for each fundamental frequency.

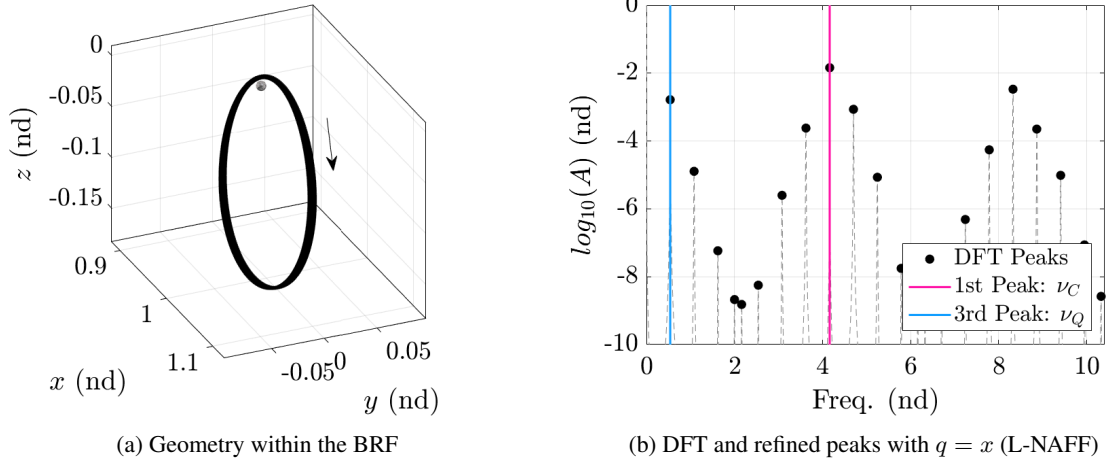


Fig. 12: Sample CR3BP quasi-NRHO

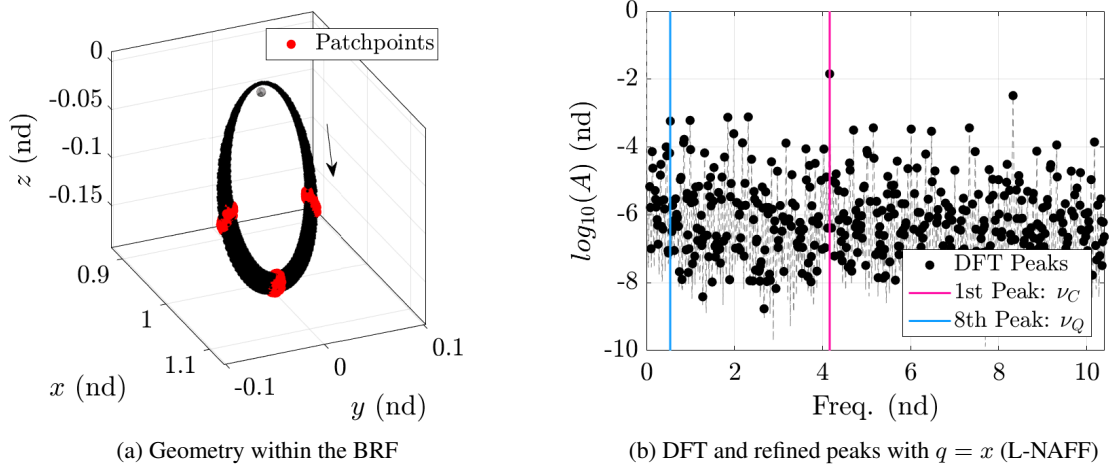


Fig. 13: HFEM quasi-NRHO prior to the targeting process

Table 11: Initial frequency structure for the NRHO in the HFEM (Fig. 13(b))

	$\nu_C (j = 1)$	$\nu_Q (j = 8)$
f_j	4.163352948064170	0.541347594980843
A_j	0.014924521456679	0.000614347272201
θ_j	0.049415700934662	3.280234288629805

Capability of the proposed FDDC approach in controlling the quasi-periodic motion within the multiple-shooting formulation is demonstrated. An *arbitrary* set of constraints on the frequency structure is formulated as follows,

$$\text{For } \nu_C : [\theta_j - 0] = 0, \quad \text{For } \nu_Q : \begin{bmatrix} A_j - 6.14347272201 \cdot 10^{-5} \\ \theta_j - \pi \end{bmatrix} = \vec{0}. \quad (89)$$

The first type of fundamental frequency, i.e., ν_C , is extremely challenging to target within the proposed multiple-shooting formulation. As the epochs (t) are assumed to be fixed, the total propagation time as well as the number of revolutions are fixed; thus, constraining ν_C results in an overconstrained problem that displays numerical sensitivities. While a variable-epoch formulation may alleviate these issue, such an avenue remains out-of-scope. For the second type of fundamental frequency, ν_Q , the amplitude is adjusted to be 1/10 of the original value as detected in Table 11. The phase angles θ_j are arbitrarily targeted as 0 and π for ν_C and ν_Q , respectively. These values are selected to be in the vicinity of the initial values (Table 11). As the continuity in the patchpoints is also targeted simultaneously, drastically changing the phase angles often results in numerical sensitivities. Thus, in practice, multiple steps may be required to reach the desired frequency structure.

Employing the frequency-domain constraints from Eq. (89) in addition to the state continuity (Eq. (84)), the initial trajectory from Fig. 13 is adjusted to another solution within the HFEM. The geometry is illustrated in Fig. 14(a). From this view, the visual difference from the initial guess in Fig. 13(a) is minimal. However, examining the frequency-domain information from Fig. 14(b), it is apparent that the amplitude associated with ν_Q is reduced. Now, while ν_C is still associated with the most dominant peak, ν_Q now tracks the 48th peak within the DFT. The targeted frequency structure is summarized in Table 12. As enforced by the constraints from Eq. (89), three frequency components are now successfully targeted. Note that as the amplitude for ν_Q decreases, it becomes increasingly challenging to refine it among other peaks as apparent from Fig. 14(b). The capabilities of the proposed FDDC for very small A_j remain an open question.

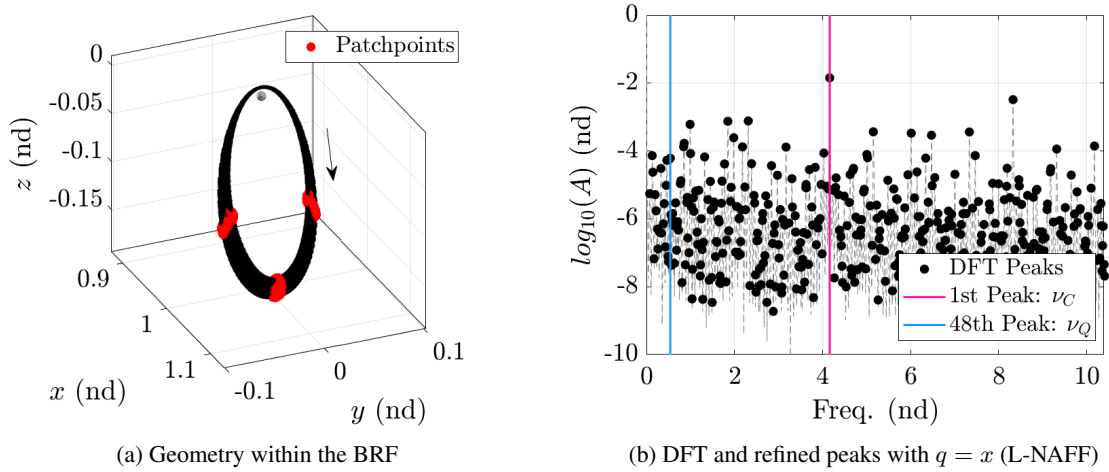


Fig. 14: HFEM quasi-NRHO with targeted frequency structure (Eq. (89))

Table 12: Targeted frequency structure for the NRHO in the HFEM from Fig. 14(b) (✓: targeted)

	$\nu_C (j = 1)$	$\nu_Q (j = 48)$
f_j	4.163383863074772	0.542683258083952
A_j	0.014924282078229	0.000061434727220 ✓
θ_j	-0.000000000000044 ✓	3.141592653577986 ✓

The proposed FDDC approach aids in specifying quasi-periodic trajectories within the HFEM. Functionally, the strategy introduces additional constraints based on the frequency-domain information, reducing the randomness in solution behavior that emanates from the underconstrained nature of the problem [47]. The approach may be applicable in scenarios where fine-tuning the solution within the HFEM is important. For example, explicitly specifying the phase angle is relevant in avoiding eclipses. Similarly, capabilities to directly control the amplitude and phase angle associated with the quasi-periodic mode (ν_Q) facilitates the relative trajectory design that leverages QPOs [49, 50, 51]. While the current analysis focuses on the 9 : 2 NRHO, the strategy is extendable to other quasi-periodic trajectories associated with inherent instability.

6 Concluding Remarks

The current study introduces the Frequency-Domain Differential Corrector (FDDC) strategy for generating multi-dimensional quasi-periodic orbits. Building on insights from existing frequency refinement methods, the approach formulates sensitivities of the frequency structure with respect to the state vector, enabling a frequency-based differential corrections process. The strategy is demonstrated in the Earth-Moon system employing both single- and multiple-shooting formulations. The modularity of the FDDC framework allows flexible integration across a range of dynamical models with evolving fidelity. By incorporating frequency-domain constraints directly into the correction process, the methodology enhances trajectory design capabilities, especially for applications involving constellations or control of oscillatory modes. Future work includes improving numerical robustness and extending the strategy to broader classes of dynamical environments and mission scenarios.

Acknowledgments

Valuable discussions with members from Multi-Body Dynamics Research Group are appreciated. Portions of this work were completed at Purdue University under Intuitive Machines LLC Award 21123283.

References

- [1] Vladimir Igorevich Arnold. *Mathematical methods of classical mechanics*, Volume 60. Springer Science & Business Media, 2013.
- [2] Victory Szebehely. *Theory of orbit: The restricted problem of three bodies*. Elsevier, 2012.
- [3] Michel Hénon. *Generating families in the restricted three-body problem*, Volume 52. Springer Science & Business Media, 1997.
- [4] Eusebius J. Doedel, Volodymyr A. Romanov, Randy C. Paffenroth, Herbert B. Keller, Donald J. Dichmann, Jorge Galán-Vioque, and André Vanderbauwhede. Elemental periodic orbits associated with the libration points in the circular restricted 3-body problem. *International Journal of Bifurcation and Chaos*, 17(08):2625–2677, 2007. doi: 10.1142/S0218127407018671.
- [5] Roger Broucke. Stability of periodic orbits in the elliptic, restricted three-body problem. *AIAA Journal*, 7(6):1003–1009, 1969. doi: 10.2514/3.5267.
- [6] Rüdiger Seydel. *Practical bifurcation and stability analysis*, Volume 5. Springer Science & Business Media, 2009.
- [7] Stephen Wiggins. *Introduction to Applied Nonlinear Dynamical Systems and Chaos*. Springer Science & Business Media, 2003.
- [8] Wang Sang Koon, Martin W. Lo, Jerrold E. Marsden, and Shane D. Ross. Dynamical systems, the three-body problem and space mission design. In *Equadiff 99: (In 2 Volumes)*, pages 1167–1181. World Scientific, 2000.
- [9] Charles C. Conley. Low energy transit orbits in the restricted three-body problems. *SIAM Journal on Applied Mathematics*, 16(4):732–746, 1968. doi: 10.1137/0116060.
- [10] Juan-Pablo Almanza-Soto and Kathleen C Howell. Itinerary prediction in the circular restricted three-body problem leveraging normal forms. In *AAS/AIAA Space Flight Mechanics Meeting, Kauai, Hawaii, January 19-23, 2025*.
- [11] Emily M. Zimovan-Spreen, Kathleen C. Howell, and Diane C. Davis. Dynamical structures nearby NRHOs with applications to transfer design in cislunar space. *The Journal of the Astronautical Sciences*, 69(3):718–744, 2022. doi: 10.1007/s40295-022-00320-4.
- [12] Àngel Jorba and Jordi Villanueva. On the persistence of lower dimensional invariant tori under quasi-periodic perturbations. *Journal of Nonlinear Science*, 7:427–473, 1997.
- [13] Gerard Gómez, Josep J. Masdemont, and Josep-Maria Mondelo. Solar system models with a selected set of frequencies. *Astronomy & Astrophysics*, 390(2):733–749, 2002. doi: 10.1051/0004-6361:20020625.

- [14] Nicola Baresi, Zubin P. Olikara, and Daniel J. Scheeres. Fully numerical methods for continuing families of quasi-periodic invariant tori in astrodynamics. *The Journal of the Astronautical Sciences*, 65: 157–182, 2018. doi: 10.1007/s40295-017-0124-6.
- [15] Gerard Gómez and Josep-Maria Mondelo. The dynamics around the collinear equilibrium points of the RTBP. *Physica D: Nonlinear Phenomena*, 157(4):283–321, 2001. doi: 10.1016/S0167-2789(01)00312-8.
- [16] Zubin P. Olikara and Daniel J. Scheeres. Numerical method for computing quasi-periodic orbits and their stability in the restricted three-body problem. *Advances in the Astronautical Sciences*, 145(911-930): 911–930, 2012.
- [17] Bhanu Kumar, Rodney L. Anderson, and Rafael de la Llave. Rapid and accurate methods for computing whiskered tori and their manifolds in periodically perturbed planar circular restricted 3-body problems. *Celestial Mechanics and Dynamical Astronomy*, 134(1):3, 2022. doi: 10.1007/s10569-021-10057-1.
- [18] Brian McCarthy. *Cislunar trajectory design methodologies incorporating quasi-periodic structures with applications*. PhD Dissertation, Purdue University, U.S., 2022.
- [19] Beom Park, Rohith Reddy Sanaga, and Kathleen C. Howell. Bridging ephemeris transition gaps: Quasi-periodic extensions for the hill restricted four-body problem in cislunar space. *Acta Astronautica*, 2025. doi: 10.1016/j.actaastro.2025.03.033v.
- [20] Nicola Baresi and Daniel Scheeres. Quasi-periodic invariant tori of time-periodic dynamical systems: Applications to small body exploration. In *Proceedings of the International Astronautical Congress*. International Astronautical Federation Guadalajara, Mexico, 2016.
- [21] Gavin Brown and Daniel Scheeres. Orbit capacity of quasi-periodic orbits around gateway. In *AAS/AIAA Space Flight Mechanics Meeting, Kauai, Hawaii, January 19-23, 2025*.
- [22] Alex Haro and Josep-Maria Mondelo. Flow map parameterization methods for invariant tori in hamiltonian systems. *Communications in Nonlinear Science and Numerical Simulation*, 101:105859, 2021. doi: 10.1016/j.cnsns.2021.105859.
- [23] Àngel Jorba and Carles Simó. On the reducibility of linear differential equations with quasiperiodic coefficients. *Journal of Differential Equations*, 98(1):111–124, 1992. doi: 10.1016/0022-0396(92)90107-X.
- [24] Álvaro Fernández-Mora, Alex Haro, and Josep-Maria Mondelo. Flow map parameterization methods for invariant tori in quasi-periodic hamiltonian systems. *SIAM Journal on Applied Dynamical Systems*, 23(1):127–166, 2024. doi: 10.1137/23M1561257.
- [25] Damennick Henry and Daniel J. Scheeres. A flow map parameterization method for quasi-periodic orbit computation in the hill restricted four-body problem. In *AAS/AIAA Astrodynamics Specialist Conference, Broomfield, Colorado, August 11-15, 2024*.
- [26] Ethan J. Dennis, Damennick B. Henry, and Daniel J. Scheeres. Exploring higher dimensional quasi-periodic orbits in the hill restricted four-body problem. In *AAS/AIAA Space Flight Mechanics Meeting, Kauai, Hawaii, January 19-23, 2025*.
- [27] Jacques Laskar. Introduction to frequency map analysis. In *Hamiltonian systems with three or more degrees of freedom*, pages 134–150. Springer, 1999. doi: 10.1007/978-94-011-4673-9_13.
- [28] Gerard Gómez, Josep-Maria Mondelo, and Carles Simó. A collocation method for the numerical fourier analysis of quasi-periodic functions. i. numerical tests and examples. *Discrete and Continuous Dynamical Systems - Series B*, 14(1):41–74, 2010. doi: 10.3934/dcdsb.2010.14.41.
- [29] Roger A. Broucke. Long-term third-body effects via double averaging. *Journal of Guidance, Control, and Dynamics*, 26(1):27–32, 2003. doi: 10.2514/2.5041.
- [30] Todd A. Ely. Stable constellations of frozen elliptical inclined lunar orbits. *The Journal of the Astronautical Sciences*, 53:301–316, 2005. doi: 10.1007/BF03546355.
- [31] David Folta and David Quinn. Lunar frozen orbits. In *AIAA/AAS Astrodynamics Specialist Conference and Exhibit*, page 6749, 2006.

- [32] David A. Vallado. *Fundamentals of astrodynamics and applications*, Volume 12. Springer Science & Business Media, 2001.
- [33] Beom Park and Kathleen C. Howell. Assessment of dynamical models for transitioning from the Circular Restricted Three-Body Problem to an ephemeris model with applications. *Celestial Mechanics and Dynamical Astronomy*, 136(6), 2024. doi: 10.1007/s10569-023-10178-9.
- [34] Ryan S. Park, William M. Folkner, James G. Williams, and Dale H. Boggs. The JPL planetary and lunar ephemerides DE440 and DE441. *The Astronomical Journal*, 161(3):105, 2021. doi: 10.3847/1538-3881/abd414.
- [35] Tao Nie and Pini Gurfil. Lunar frozen orbits revisited. *Celestial Mechanics and Dynamical Astronomy*, 130(10):61, 2018. doi: 10.1007/s10569-018-9858-0.
- [36] James M. Longuski, Felix R. Hoots, and George E. Pollock IV. *Introduction to Orbital Perturbations*, Volume 40. Springer Nature, 2022.
- [37] Richard G. Lyons. *Understanding digital signal processing*, 3/E. Pearson, 1997.
- [38] Gerard Gómez, Josep-Maria Mondelo, and Carles Simó. A collocation method for the numerical fourier analysis of quasi-periodic functions. II. analytical error estimates. *Discrete and Continuous Dynamical Systems - Series B*, 14(1):75–109, 2010. doi: 10.3934/dcdsb.2010.14.75.
- [39] Alessandro Morbidelli and Antonio Giorgilli. Superexponential stability of KAM tori. *Journal of Statistical Physics*, 78:1607–1617, 1995. doi: 10.1007/BF02180145.
- [40] Collin Bezrouk and Jeffrey S. Parker. Long term evolution of distant retrograde orbits in the earth-moon system. *Astrophysics and Space Science*, 362:1–11, 2017. doi: 10.1007/s10509-017-3158-0.
- [41] Brian Baker-McEvilly, Surabhi Bhadauria, David Canales, and Carolin Frueh. A comprehensive review on cislunar expansion and space domain awareness. *Progress in Aerospace Sciences*, 147:101019, 2024. doi: 10.1016/j.paerosci.2024.101019.
- [42] Antonio Fernando Bertachini Almeida Prado. Third-body perturbation in orbits around natural satellites. *Journal of Guidance, Control, and Dynamics*, 26(1):33–40, 2003. doi: 10.2514/2.5042.
- [43] K. C. Howell, D. J. Grebow, and Z. P. Olikara. Design using gauss’ perturbing equations with applications to lunar south pole coverage. In *AAS/AIAA Space Flight Mechanics Meeting, Sedona, Arizona, January 28-February 1, 2007*.
- [44] Todd A. Ely and Erica Lieb. Constellations of elliptical inclined lunar orbits providing polar and global coverage. *The Journal of the Astronautical Sciences*, 54(1):53–67, 2006. doi: 10.1007/BF03256476.
- [45] Kenshiro Oguri, Kenta Oshima, Stefano Campagnola, Kota Kakihara, Naoya Ozaki, Nicola Baresi, Yasuhiro Kawakatsu, and Ryu Funase. Equuleus trajectory design. *The Journal of the Astronautical Sciences*, 67(3):950–976, 2020. doi: 10.1007/s40295-019-00206-y.
- [46] Natasha Bosanac, Andrew D. Cox, Kathleen C. Howell, and David C. Folta. Trajectory design for a cislunar cubesat leveraging dynamical systems techniques: The lunar icecube mission. *Acta Astronautica*, 144:283–296, 2018. doi: 10.1016/j.actaastro.2017.12.025.
- [47] Diogene A. Dei Tos and Francesco Topputo. Trajectory refinement of three-body orbits in the real solar system model. *Advances in Space Research*, 59(8):2117–2132, 2017. doi: 10.1016/j.asr.2017.01.039.
- [48] Emily M. Zimovan-Spreen, Stephen T. Scheuerle, Brian P. McCarthy, Diane C. Davis, and Kathleen C. Howell. Baseline orbit generation for near rectilinear halo orbits. In *AAS/AIAA Astrodynamics Specialist Conference, Big Sky, Montana, August 13-17, 2023*.
- [49] Damennick B. Henry and Daniel J. Scheeres. Expansion maps: Designing relative trajectories on quasi-periodic orbits. *Journal of Guidance, Control, and Dynamics*, 44(3):457–468, 2021. doi: 10.2514/1.G005492.
- [50] Mitchell Dominguez and Kathleen C. Howell. Preliminary design strategy for long-term loitering orbits in cislunar space. In *AAS/AIAA Astrodynamics Specialist Conference, Broomfield, Colorado, August 11-15, 2024*.

- [51] Andrea Capannolo, Giovanni Zanotti, Michèle Lavagna, and Giuseppe Cataldo. Model predictive control for formation reconfiguration exploiting quasi-periodic tori in the cislunar environment. *Nonlinear Dynamics*, 111(8):6941–6959, 2023. doi: 10.1007/s11071-022-08214-8.

Appendix A: Jacobian Matrix Components for the Refinement Strategies

L-NAFF

Each component of the Jacobian matrix (Eq. (49)) for the L-NAFF is rendered as,

$$\begin{aligned} \frac{\partial F_{L,\mathbf{f}}}{\partial \mathbf{f}_j} = & -\frac{1}{2\sqrt{\mathcal{C}_q(\mathbf{f}_j)^2 + \mathcal{S}_q(\mathbf{f}_j)^2}^3} \left(\mathcal{C}_q(\mathbf{f}_j) \frac{d\mathcal{C}_q(\mathbf{f}_j)}{d\mathbf{f}_j} + \mathcal{S}_q(\mathbf{f}_j) \frac{d\mathcal{S}_q(\mathbf{f}_j)}{d\mathbf{f}_j} \right)^2 \\ & + \frac{1}{2\sqrt{\mathcal{C}_q(\mathbf{f}_j)^2 + \mathcal{S}_q(\mathbf{f}_j)^2}} \left(\left(\frac{d\mathcal{C}_q(\mathbf{f}_j)}{d\mathbf{f}_j} \right)^2 + \left(\frac{d\mathcal{S}_q(\mathbf{f}_j)}{d\mathbf{f}_j} \right)^2 + \mathcal{C}_q(\mathbf{f}_j) \frac{d^2\mathcal{C}_q(\mathbf{f}_j)}{d\mathbf{f}_j^2} + \mathcal{S}_q(\mathbf{f}_j) \frac{d^2\mathcal{S}_q(\mathbf{f}_j)}{d\mathbf{f}_j^2} \right) \end{aligned} \quad (90)$$

$$\frac{\partial F_{L,\mathbf{f}}}{\partial A_j} = 0 \quad (91)$$

$$\frac{\partial F_{L,\mathbf{f}}}{\partial \theta_j} = 0 \quad (92)$$

$$\frac{\partial F_{L,\mathcal{C}}}{\partial \mathbf{f}_j} = A_j \cos \theta_j \frac{d\mathcal{C}_{c(\mathbf{f}_j)}(\mathbf{f}_j)}{d\mathbf{f}_j} - A_j \sin \theta_j \frac{d\mathcal{C}_{s(\mathbf{f}_j)}(\mathbf{f}_j)}{d\mathbf{f}_j} - \frac{d\mathcal{C}_q(\mathbf{f}_j)}{d\mathbf{f}_j} \quad (93)$$

$$\frac{\partial F_{L,\mathcal{C}}}{\partial A_j} = \cos \theta_j \mathcal{C}_{c(\mathbf{f}_j)}(\mathbf{f}_j) - \sin \theta_j \mathcal{C}_{s(\mathbf{f}_j)}(\mathbf{f}_j) \quad (94)$$

$$\frac{\partial F_{L,\mathcal{C}}}{\partial \theta_j} = -A_j \sin \theta_j \mathcal{C}_{c(\mathbf{f}_j)}(\mathbf{f}_j) - A_j \cos \theta_j \mathcal{C}_{s(\mathbf{f}_j)}(\mathbf{f}_j) \quad (95)$$

$$\frac{\partial F_{L,\mathcal{S}}}{\partial \mathbf{f}_j} = A_j \cos \theta_j \frac{d\mathcal{S}_{c(\mathbf{f}_j)}(\mathbf{f}_j)}{d\mathbf{f}_j} - A_j \sin \theta_j \frac{d\mathcal{S}_{s(\mathbf{f}_j)}(\mathbf{f}_j)}{d\mathbf{f}_j} - \frac{d\mathcal{S}_q(\mathbf{f}_j)}{d\mathbf{f}_j} \quad (96)$$

$$\frac{\partial F_{L,\mathcal{S}}}{\partial A_j} = \cos \theta_j \mathcal{S}_{c(\mathbf{f}_j)}(\mathbf{f}_j) - \sin \theta_j \mathcal{S}_{s(\mathbf{f}_j)}(\mathbf{f}_j) \quad (97)$$

$$\frac{\partial F_{L,\mathcal{S}}}{\partial \theta_j} = -A_j \sin \theta_j \mathcal{S}_{c(\mathbf{f}_j)}(\mathbf{f}_j) - A_j \cos \theta_j \mathcal{S}_{s(\mathbf{f}_j)}(\mathbf{f}_j). \quad (98)$$

Note the following additional quantities,

$$\frac{d^2\mathcal{C}_q(\mathbf{f}_j)}{d\mathbf{f}_j^2} = \frac{2}{N} \sum_{i=0}^{N-1} t_i^2 q(t_i) h(i) (-\cos(\mathbf{f}_j t_i)) \quad (99)$$

$$\frac{d^2\mathcal{S}_q(\mathbf{f}_j)}{d\mathbf{f}_j^2} = \frac{2}{N} \sum_{i=0}^{N-1} t_i^2 q(t_i) h(i) (-\sin(\mathbf{f}_j t_i)) \quad (100)$$

$$\frac{d\mathcal{C}_{c(\mathbf{f}_j)}(\mathbf{f}_j)}{d\mathbf{f}_j} = -\frac{d\mathcal{S}_{s(\mathbf{f}_j)}(\mathbf{f}_j)}{d\mathbf{f}_j} = \frac{2}{N} \sum_i^{N-1} (-2t_i \sin(\mathbf{f}_j t_i) \cos(t_i \mathbf{f}_j) h(i)) \quad (101)$$

$$\frac{d\mathcal{S}_{c(\mathbf{f}_j)}(\mathbf{f}_j)}{d\mathbf{f}_j} = \frac{2}{N} \sum_i^{N-1} (-t_i (\sin(\mathbf{f}_j))^2 h(i) + t_i (\cos(\mathbf{f}_j t_i))^2 h(i)). \quad (102)$$

GMS-C

The components from the Jacobian matrix (Eq. (65)) are provided as,

$$\frac{\partial F_{G,C(\omega_k^{*j})}}{\partial \mathbf{f}_j} = A_j \cos \theta_j \frac{d\mathcal{C}_{c(\mathbf{f}_j)}(\omega_k^{*j})}{d\mathbf{f}_j} - A_j \sin \theta_j \frac{d\mathcal{C}_{s(\mathbf{f}_j)}(\omega_k^{*j})}{d\mathbf{f}_j} \quad (103)$$

$$\frac{\partial F_{G,C(\omega_k^{*j})}}{\partial A_j} = \cos \theta_j \mathcal{C}_{c(\mathbf{f}_j)}(\omega_k^{*j}) - \sin \theta_j \mathcal{C}_{s(\mathbf{f}_j)}(\omega_k^{*j}) \quad (104)$$

$$\frac{\partial F_{G,C(\omega_k^{*j})}}{\partial \theta_j} = -A_j \sin \theta_j \mathcal{C}_{c(\mathbf{f}_j)}(\omega_k^{*j}) - A_j \cos \theta_j \mathcal{C}_{s(\mathbf{f}_j)}(\omega_k^{*j}) \quad (105)$$

$$\frac{\partial F_{G,S(\omega_k^{*j})}}{\partial \mathbf{f}_j} = A_j \cos \theta_j \frac{d\mathcal{S}_{c(\mathbf{f}_j)}(\omega_k^{*j})}{d\mathbf{f}_j} - A_j \sin \theta_j \frac{d\mathcal{S}_{s(\mathbf{f}_j)}(\omega_k^{*j})}{d\mathbf{f}_j} \quad (106)$$

$$\frac{\partial F_{G,S(\omega_k^{*j})}}{\partial A_j} = \cos \theta_j \mathcal{S}_{c(\mathbf{f}_j)}(\omega_k^{*j}) - \sin \theta_j \mathcal{S}_{s(\mathbf{f}_j)}(\omega_k^{*j}) \quad (107)$$

$$\frac{\partial F_{G,C(\omega_k^{*j})}}{\partial \theta_j} = -A_j \sin \theta_j \mathcal{S}_{c(\mathbf{f}_j)}(\omega_k^{*j}) - A_j \cos \theta_j \mathcal{S}_{s(\mathbf{f}_j)}(\omega_k^{*j}) \quad (108)$$

$$\frac{\partial F_{G,CS(\omega_{k\pm 1}^{*j})}}{\partial \mathbf{f}_j} = A_j \cos \theta_j \frac{d\mathcal{CS}_{c(\mathbf{f}_j)}(\omega_{k\pm 1}^{*j})}{d\mathbf{f}_j} - A_j \sin \theta_j \frac{d\mathcal{CS}_{s(\mathbf{f}_j)}(\omega_{k\pm 1}^{*j})}{d\mathbf{f}_j} \quad (109)$$

$$\frac{\partial F_{G,CS(\omega_{k\pm 1}^{*j})}}{\partial A_j} = \cos \theta_j \mathcal{CS}_{c(\mathbf{f}_j)}(\omega_{k\pm 1}^{*j}) - \sin \theta_j \mathcal{CS}_{s(\mathbf{f}_j)}(\omega_{k\pm 1}^{*j}) \quad (110)$$

$$\frac{\partial F_{G,CS(\omega_{k\pm 1}^{*j})}}{\partial \theta_j} = -A_j \sin \theta_j \mathcal{CS}_{c(\mathbf{f}_j)}(\omega_{k\pm 1}^{*j}) - A_j \cos \theta_j \mathcal{CS}_{s(\mathbf{f}_j)}(\omega_{k\pm 1}^{*j}). \quad (111)$$

The ambiguity in \mathcal{CS} for $\omega_{k\pm 1}^{*j}$ is resolved via comparing the norm of the inverse for the Jacobians constructed with \mathcal{C} and \mathcal{S} for $\omega_{k\pm 1}^{*j}$; the one with smaller norm is selected to supply a better conditioned matrix inverse [38].

Appendix B: Sensitivity Vector Components for the Single-Shooting Formulation

L-NAFF

The vector components in the right-side of Eq. (71) are supplied as,

$$\frac{\partial F_{L,\mathbf{f}}}{\partial \vec{\mathbf{X}}_0} = -\frac{1}{2\sqrt{\mathcal{C}_q(\mathbf{f}_j)^2 + \mathcal{S}_q(\mathbf{f}_j)^2}^3} L_1 L_2 + \frac{1}{2\sqrt{\mathcal{C}_q(\mathbf{f}_j)^2 + \mathcal{S}_q(\mathbf{f}_j)^2}} (L_3 + L_4), \quad (112)$$

where,

$$L_1 = \left(\mathcal{C}_q(\mathbf{f}_j) \frac{d\mathcal{C}_q(\mathbf{f}_j)}{d\mathbf{f}_j} + \mathcal{S}_q(\mathbf{f}_j) \frac{d\mathcal{S}_q(\mathbf{f}_j)}{d\mathbf{f}_j} \right) \quad (113)$$

$$L_2 = \left(\mathcal{C}_q(\mathbf{f}_j) \frac{\partial \mathcal{C}_q(\mathbf{f}_j)}{\partial \vec{\mathbf{X}}_0} + \mathcal{S}_q(\mathbf{f}_j) \frac{\partial \mathcal{S}_q(\mathbf{f}_j)}{\partial \vec{\mathbf{X}}_0} \right) \quad (114)$$

$$L_3 = \left(\frac{\partial \mathcal{C}_q(\mathbf{f}_j)}{\partial \vec{\mathbf{X}}_0} \right) \left(\frac{d\mathcal{C}_q(\mathbf{f}_j)}{d\mathbf{f}_j} \right) + \left(\frac{\partial \mathcal{S}_q(\mathbf{f}_j)}{\partial \vec{\mathbf{X}}_0} \right) \left(\frac{d\mathcal{S}_q(\mathbf{f}_j)}{d\mathbf{f}_j} \right) \quad (115)$$

$$L_4 = \mathcal{C}_q(\mathbf{f}_j) \frac{\partial}{\partial \vec{\mathbf{X}}_0} \left(\frac{d\mathcal{C}_q(\mathbf{f}_j)}{d\mathbf{f}_j} \right) + \mathcal{S}_q(\mathbf{f}_j) \frac{\partial}{\partial \vec{\mathbf{X}}_0} \left(\frac{d\mathcal{S}_q(\mathbf{f}_j)}{d\mathbf{f}_j} \right). \quad (116)$$

Additionally,

$$-\frac{\partial F_{L,C}}{\partial \vec{\mathbb{X}}_0} = \frac{\partial \mathcal{C}_q(\mathbf{f}_j)}{\partial \vec{\mathbb{X}}_0} \quad (117)$$

$$-\frac{\partial F_{L,S}}{\partial \vec{\mathbb{X}}_0} = \frac{\partial \mathcal{S}_q(\mathbf{f}_j)}{\partial \vec{\mathbb{X}}_0}, \quad (118)$$

where,

$$\frac{\partial \mathcal{D}_q(\mathbf{f}_j)}{\partial \vec{\mathbb{X}}_0} = \frac{1}{N} \sum_{i=0}^{N-1} \left(\frac{dq(t_i)}{d\vec{\mathbb{X}}_0} h(i) (\cos(\mathbf{f}_j t_i) - \mathbf{i} \sin(\mathbf{f}_j t_i)) \right) = \frac{1}{2} \frac{\partial \mathcal{C}_q(\mathbf{f}_j)}{\partial \vec{\mathbb{X}}_0} - \mathbf{i} \frac{1}{2} \frac{\partial \mathcal{S}_q(\mathbf{f}_j)}{\partial \vec{\mathbb{X}}_0}. \quad (119)$$

Most terms are supplied from Sect. 3 except for,

$$\frac{\partial}{\partial \vec{\mathbb{X}}_0} \left(\frac{d\mathcal{C}_q(\mathbf{f}_j)}{d\mathbf{f}_j} \right) = \frac{2}{N} \sum_{i=0}^{N-1} t_i \frac{dq(t_i)}{d\vec{\mathbb{X}}_0} h(i) (-\sin(\mathbf{f}_j t_i)) \quad (120)$$

$$\frac{\partial}{\partial \vec{\mathbb{X}}_0} \left(\frac{d\mathcal{S}_q(\mathbf{f}_j)}{d\mathbf{f}_j} \right) = \frac{2}{N} \sum_{i=0}^{N-1} t_i \frac{dq(t_i)}{d\vec{\mathbb{X}}_0} h(i) (\cos(\mathbf{f}_j t_i)), \quad (121)$$

with $\frac{dq(t_i)}{d\vec{\mathbb{X}}_0} = \frac{dq(t_i)}{d\vec{\mathbb{X}}^{t_i}(\vec{\mathbb{X}}_0; \mathbf{t}_0)} \phi^{t_i}(\vec{\mathbb{X}}_0; \mathbf{t}_0)$, concluding the derivations for the L-NAFF.

GMS-C

Evaluation of the right-side of Eq. (73) requires the following derivative (from Eq. (20)),

$$\frac{\partial \mathcal{D}_q(\omega_k^{*j})}{\partial \vec{\mathbb{X}}_0} = \frac{1}{N} \sum_{i=0}^{N-1} \left(\frac{dq(t_i)}{d\vec{\mathbb{X}}_0} h(i) (\cos(\omega_k^{*j} t_i) - \mathbf{i} \sin(\omega_k^{*j} t_i)) \right) \quad (122)$$

$$= \frac{1}{N} \sum_{i=0}^{N-1} \left(\frac{dq(t_i)}{d\vec{\mathbb{X}}^{t_i}(\vec{\mathbb{X}}_0; \mathbf{t}_0)} \phi^{t_i}(\vec{\mathbb{X}}_0; \mathbf{t}_0) h(i) (\cos(\omega_k^{*j} t_i) - \mathbf{i} \sin(\omega_k^{*j} t_i)) \right). \quad (123)$$

Then, the real and imaginary components constitute the right-side of Eq. (73), concluding the derivations.

Appendix C: Sensitivity Vector Components for the Multiple-Shooting Formulation

L-NAFF

The equation from the single-shooting formulation (Eq. (112)) is trivially extended. The process requires following vectors,

$$\frac{\partial \mathcal{D}_q(\mathbf{f}_j)}{\partial \vec{\mathbb{X}}} = \begin{bmatrix} \frac{\partial \mathcal{D}_q(\mathbf{f}_j)}{\partial \vec{\mathbb{X}}_0} & \frac{\partial \mathcal{D}_q(\mathbf{f}_j)}{\partial \vec{\mathbb{X}}_1} & \cdots & \frac{\partial \mathcal{D}_q(\mathbf{f}_j)}{\partial \vec{\mathbb{X}}_{n_p-1}} \end{bmatrix} \quad (124)$$

$$\frac{\partial}{\partial \vec{\mathbb{X}}} \left(\frac{d\mathcal{C}_q(\mathbf{f}_j)}{d\mathbf{f}_j} \right) = \begin{bmatrix} \frac{\partial}{\partial \vec{\mathbb{X}}_0} \left(\frac{d\mathcal{C}_q(\mathbf{f}_j)}{d\mathbf{f}_j} \right) & \frac{\partial}{\partial \vec{\mathbb{X}}_1} \left(\frac{d\mathcal{C}_q(\mathbf{f}_j)}{d\mathbf{f}_j} \right) & \cdots & \frac{\partial}{\partial \vec{\mathbb{X}}_{n_p}} \left(\frac{d\mathcal{C}_q(\mathbf{f}_j)}{d\mathbf{f}_j} \right) \end{bmatrix} \quad (125)$$

$$\frac{\partial}{\partial \vec{\mathbb{X}}} \left(\frac{d\mathcal{S}_q(\mathbf{f}_j)}{d\mathbf{f}_j} \right) = \begin{bmatrix} \frac{\partial}{\partial \vec{\mathbb{X}}_0} \left(\frac{d\mathcal{S}_q(\mathbf{f}_j)}{d\mathbf{f}_j} \right) & \frac{\partial}{\partial \vec{\mathbb{X}}_1} \left(\frac{d\mathcal{S}_q(\mathbf{f}_j)}{d\mathbf{f}_j} \right) & \cdots & \frac{\partial}{\partial \vec{\mathbb{X}}_{n_p-1}} \left(\frac{d\mathcal{S}_q(\mathbf{f}_j)}{d\mathbf{f}_j} \right) \end{bmatrix}. \quad (126)$$

Each element is evaluated as,

$$\frac{\partial \mathcal{D}_q(\mathbf{f}_j)}{\partial \vec{\mathbb{X}}_{i_p}} = \frac{1}{|\mathcal{I}|} \sum_{i \in \mathcal{I}} \left(\frac{dq(t_i)}{d\vec{\mathbb{X}}^{t_i - \mathbf{t}_{i_p}}(\vec{\mathbb{X}}_{i_p}; \mathbf{t}_{i_p})} \phi^{t_i - \mathbf{t}_{i_p}}(\vec{\mathbb{X}}_{i_p}; \mathbf{t}_{i_p}) h(i) (\cos(\mathbf{f}_j t_i) - \mathbf{i} \sin(\mathbf{f}_j t_i)) \right) \quad (127)$$

$$\frac{\partial}{\partial \vec{\mathbb{X}}_{i_p}} \left(\frac{d\mathcal{C}_q(\mathbf{f}_j)}{d\mathbf{f}_j} \right) = \frac{2}{|\mathcal{I}|} \sum_{i \in \mathcal{I}} t_i \frac{dq(t_i)}{d\vec{\mathbb{X}}^{t_i - \mathbf{t}_{i_p}}(\vec{\mathbb{X}}_{i_p}; \mathbf{t}_{i_p})} \phi^{t_i - \mathbf{t}_{i_p}}(\vec{\mathbb{X}}_{i_p}; \mathbf{t}_{i_p}) h(i) (-\sin(\mathbf{f}_j t_i)) \quad (128)$$

$$\frac{\partial}{\partial \vec{\mathbb{X}}_{i_p}} \left(\frac{d\mathcal{S}_q(\mathbf{f}_j)}{d\mathbf{f}_j} \right) = \frac{2}{|\mathcal{I}|} \sum_{i \in \mathcal{I}} t_i \frac{dq(t_i)}{d\vec{\mathbb{X}}^{t_i - \mathbf{t}_{i_p}}(\vec{\mathbb{X}}_{i_p}; \mathbf{t}_{i_p})} \phi^{t_i - \mathbf{t}_{i_p}}(\vec{\mathbb{X}}_{i_p}; \mathbf{t}_{i_p}) h(i) (\cos(\mathbf{f}_j t_i)), \quad (129)$$

where the index vector \mathcal{I} is defined as, $\mathcal{I} = \{i \mid \mathbf{t}_{i_p} \leq t_i < \mathbf{t}_{i_p+1}\}$ and $|\mathcal{I}|$ is the length of the vector. Equations (127)-(129) are evaluated for $0 \leq i_p < n_p - 1$. This process concludes the extension of FDDC into the multiple-shooting formulation leveraging the L-NAFF approach.

GMS-C

Evaluation of the right-side of Eq. (73) requires the following derivative (from Eq. (20)),

$$\frac{\partial \mathcal{D}_q(\omega_k^{*j})}{\partial \vec{\mathbb{X}}} = \begin{bmatrix} \frac{d\mathcal{D}_q(\omega_k^{*j})}{d\vec{\mathbb{X}}_0} & \frac{d\mathcal{D}_q(\omega_k^{*j})}{d\vec{\mathbb{X}}_1} & \dots & \frac{d\mathcal{D}_q(\omega_k^{*j})}{d\vec{\mathbb{X}}_{n_p-1}} \end{bmatrix}, \quad (130)$$

where,

$$\frac{\partial \mathcal{D}_q(\omega_k^{*j})}{\partial \vec{\mathbb{X}}_{i_p}} = \frac{1}{|\mathcal{I}|} \sum_{i \in \mathcal{I}} \left(\frac{dq(t_i)}{d\vec{\mathbb{X}}^{t_i - \mathbf{t}_{i_p}}(\vec{\mathbb{X}}_{i_p}; \mathbf{t}_{i_p})} \phi^{t_i - \mathbf{t}_{i_p}}(\vec{\mathbb{X}}_{i_p}; \mathbf{t}_{i_p}) h(i) (\cos(\omega_k^{*j} t_i) - \mathbf{i} \sin(\omega_k^{*j} t_i)) \right), \quad (131)$$

for $0 \leq i_p < n_p - 1$, concluding the derivations.